

Dilute suspension of neutrally buoyant particles in viscoelastic turbulent channel flow

Amir Esteghamatian¹ and Tamer A. Zaki^{1,†}

¹Department of Mechanical Engineering, Johns Hopkins University, Baltimore, MD 21218, USA

(Received 18 February 2019; revised 8 June 2019; accepted 9 June 2019;
first published online 18 July 2019)

Direct numerical simulations of viscoelastic turbulent channel flow laden with neutrally buoyant spherical particles are performed. Two FENE-P viscoelastic and one Newtonian fluid are examined, and for each the particle-laden configuration is contrasted to a reference condition without seeding. The size of the particles is larger than the dissipation length scale, and their presence enhances drag in a manner that is intrinsically different in the viscoelastic and Newtonian flows. While the particles effectively suppress the turbulence activity, they significantly enhance the polymer stresses. The polymer chains are markedly stretched in the vicinity of the particles, altering the correlation between the turbulence and polymer work that is commonly observed in single-phase viscoelastic turbulence. At the lower elasticity, the particles enhance the cycle of hibernating and active turbulence and, in turn, their migration and volume-fraction profiles are qualitatively altered by the intermittency of the turbulence. Particle–fluid momentum transfer is investigated by estimating the local fluid field on a trimmed spherical shell around the individual particles. And by comparing the particle microstructures, a lower probability of particle alignment in the streamwise direction is observed in the viscoelastic configuration. This effect is attributed to a qualitative difference in the conditionally averaged velocity fields in the vicinity of the particles in the Newtonian and viscoelastic flows.

Key words: particle/fluid flow, polymers, turbulence simulation

1. Introduction

Polymer solutions have been widely used for drag reduction in numerous industrial and environmental applications (Silberman 1983). In many instances, a dispersed phase is either intentionally or undesirably present (Doan *et al.* 1998; Barbati *et al.* 2016). The combined effects of viscoelasticity, the dispersed phase and turbulence are mostly unexplored, and render the dynamics of such flows acutely complex. Previous efforts focused on either one of these elements or the interplay of two. In the present study, we perform direct numerical simulations of viscoelastic and Newtonian turbulent channel flows without and with the dispersed phase. All three effects are therefore present in the simulations and are analysed in detail.

† Email address for correspondence: t.zaki@jhu.edu

1.1. Viscoelastic turbulent flows

Since the early findings by Toms (1948) that polymer additives can reduce drag, the interactions of viscoelasticity and turbulence have been extensively studied (Lumley 1969; White & Mungal 2008). When the time scale of the polymer stretch and relaxation, λ , is comparable to that of the turbulence, polymer chains absorb and release energy at different spatial and temporal flow scales, disrupt the natural regeneration cycle of wall turbulence and reduce drag (White & Mungal 2008). At intermediate levels of drag reduction, the near-wall vortices are damped but the streamwise fluctuations are enhanced (Dubief *et al.* 2004). At higher levels, the streamwise velocity fluctuations diminish and the log-layer mean-velocity gradient is markedly modified. Dallas, Vassilicos & Hewitt (2010) also confirmed that streamwise fluctuations weaken as the maximum drag reduction (MDR) state is approached (Virk, Mickley & Smith 1970). Hairpin packets are also suppressed with increasing elasticity (Kim *et al.* 2008; Kim & Sureshkumar 2013). The structural changes in the turbulent structures are most evident in bypass and natural transition: streaks are stabilized (Agarwal, Brandt & Zaki 2014; Biancofiore, Brandt & Zaki 2017) and Λ -structures suppressed (Lee & Zaki 2017). While beyond the present scope, it is noteworthy that the MDR bound has recently been challenged; the flow is shown to re-laminarize prior to the MDR state (Choueiri, Lopez & Hof 2018).

The observations from simulations and experiments motivated recent theoretical studies. Page & Zaki (2014) derived the linear evolution equations governing the vorticity and polymer-torque perturbations in Oldroyd-B fluids, and classified streaks as quasi-Newtonian, elastic or inertio-elastic depending on the ratio of the viscous diffusion and relaxation time scales. Page & Zaki (2015) studied the evolution of a spanwise vortex in mean shear and discovered a reverse-Orr amplification mechanism: perturbation in the polymer torque amplify when they are aligned with the background shear, in contrast to Newtonian flows where the streamfunction only amplifies if there is a net tilt against the shear. White, Dubief & Klewicki (2018) argued that the dominance of the viscous term in viscoelastic turbulence is due to eradicated inertial mechanisms, and not an increase in apparent viscosity.

The literature on the interaction of a dispersed phase with viscoelastic fluids is mostly limited to dilute concentrations of particles in laminar flows and the rheological properties of suspensions (Scirocco, Vermant & Mewis 2005; Greco, D'Avino & Maffettone 2007; Einarsson, Yang & Shaqfeh 2018). Studies dedicated to turbulence are also in the dilute limit and the particles are smaller than the Kolmogorov length scale, or in the one-way coupling regime (De Lillo, Boffetta & Musacchio 2012; Nowbahar *et al.* 2013). Very recently, Zade, Lundell & Brandt (2019) experimentally contrasted the particle–turbulence interactions in a duct flow in both Newtonian and viscoelastic conditions. They reported that the viscoelastic drag reduction is less effective in the presence of particles and attributed this effect to the increased particle stresses. Except for that recent study, the modification of viscoelastic turbulence by finite-size particles is largely unexplored. As a result, it is not possible to anticipate the effect of the solid phase on interesting phenomenology such as the alternation of viscoelastic wall turbulence between active and hibernating states (Xi & Graham 2010) or, even more generally, on the capacity of viscoelasticity to reduce turbulence drag.

1.2. Particle-laden turbulent flows

The interaction of a solid phase and Newtonian turbulence depends on numerous parameters including the particle size, density ratio, concentration, shape and

angularity, deformability, etc. (see Balachandar & Eaton 2010, for a review). When the particle size is of the order of the dissipation length scale, the flow is locally Stokesian. In this regime, the Stokes number, defined as the ratio of the particle response time to the Kolmogorov time scale, determines the modulation of turbulence by particles at a fixed particle volume and mass ratio; particles with large response time enhance the decay rate of kinetic energy in isotropic turbulence by exerting a counter-torque on a local eddy (Ferrante & Elghobashi 2003). In extremely dilute concentrations in wall turbulence, Pan & Banerjee (1996) reported that the particles attenuate the Reynolds stress by weakening the ejection–sweep cycles. Marchioli & Soldati (2002) showed that sweeping motions push the particles from high-speed streaks towards the wall, while ejections entrain the near-wall particles towards the outer layer. The relative dominance of the former effect promotes the influx of particles towards the wall – a phenomenon known as turbophoresis drift (Caporaloni *et al.* 1975) which is reportedly attenuated by viscoelasticity due to the weaker wall-normal fluctuations (Nowbahar *et al.* 2013). It is also noteworthy that both numerical (Pan & Banerjee 1997) and experimental (Kaftori, Hetsroni & Banerjee 1994) studies of Newtonian wall turbulence predict that particles smaller than the dissipation length scale preferentially reside in low-speed near-wall streaks.

Finite-size particles, of the order of the Taylor length scale, markedly alter the above picture. According to Lucci, Ferrante & Elghobashi (2011), identical particle response time and concentration but different sizes can lead to different effects on the turbulent structures. Therefore, the Stokes number cannot alone determine the particle–turbulence interaction. Naso & Prosperetti (2010) demonstrated that for such particle sizes, the turbulence is modulated at distances larger than ten times the thickness of the particle boundary layer – approximately twice the particle diameter. Cisse, Homann & Bec (2013) examined the local turbulence modulation in the vicinity of an isolated particle and concluded that the turbulence is promoted in most directions, but markedly tamed downstream. In channel flow with dilute suspension (2–5 %) of neutrally buoyant particles, Shao, Wu & Yu (2012) and Picano, Breugem & Brandt (2015) reported that particles weaken the streamwise streaks, enhance the cross-stream fluctuations and on the whole increase drag. At higher particle concentration (~20 %), the turbulent fluctuations in all directions are reduced in the buffer and log layers, and the total drag is further increased: the contribution of the particle stress to the total drag is thus sufficiently high to negate the reduction in the turbulent shear stress (Picano *et al.* 2015). It is important to note that the contribution of the particle stress to the total drag is not simply a rheological effect due to increased bulk apparent viscosity: Costa *et al.* (2018) cross-compared direct numerical simulations (DNS) of semi-dilute neutrally buoyant spheres in a channel with a Newtonian single-phase configuration with matching apparent viscosity; they showed that the contribution of the particles to the total drag in the laden case originates primarily from the particles creating local shear-rate hotspots, particularly in the near-wall region.

Particle migration, which can appreciably modify wall-bounded shear flows, is influenced by various parameters. For example, in Newtonian inertial laminar flow, the early work by Segre & Silberberg (1961) documented the radial migration of isolated finite-size particles towards an equilibrium position in a straight tube. As the Reynolds number increases, the equilibrium position shifts outwardly towards the wall (Matas, Morris & Guazzelli 2004). Another important phenomenon is near-wall layering of neutrally buoyant spherical particles in both laminar and turbulent Newtonian channel flows (Yeo & Maxey 2011; Lashgari *et al.* 2016). This effect is often explained

by wall lubrication and asymmetric interaction of near-wall particles (Picano *et al.* 2015). Costa *et al.* (2016) characterized the wall layer by an effective wall location and claimed that the dynamics in the outer flow is well described by a single-phase fluid with a matched apparent viscosity. Fornari *et al.* (2016) assessed the impact of particle inertia and size ratio on layering; at a density ratio ~ 10 they reported collision-induced migration towards the channel centre which they attributed to the near-wall asymmetry. In a very similar configuration, Yu *et al.* (2017) indicated that the same trend persists at very dilute concentrations and is therefore not collision induced. Both studies agreed that at extreme density ratio (~ 1000), particle motion expectedly tends to that of a colloidal Brownian movement irrespective of the background fluid. An example where the wall layer is depleted is in suspension of neutrally buoyant oblate or prolate spheroids in Newtonian channel flow (Ardekani & Brandt 2019).

Particle migration in laminar shear flows is known to be influenced by viscoelasticity; it is curious whether and how it is altered in the case of a viscoelastic turbulence. Early experiments in the laminar regime by Karnis & Mason (1966) reported that normal stress differences drive an isolated particle towards the channel centre. Motivated by applications in microfluidic devices, numerous efforts have since examined the migration of isolated particles in different non-Newtonian conditions, mostly in the absence of inertia (see D'Avino, Greco & Maffettone 2017, for a review). More recently, both experimental and numerical studies (e.g. Lim *et al.* 2014; Li, Karimi & Ardekani 2014) reported that migration towards the channel centre is also observed in viscoelastic inertial flows.

In the present study, we examine the simultaneous effects of dispersed phase, viscoelasticity and turbulence by DNS. The computations resolve the flow and polymer conformation fields of viscoelastic turbulence laden with finite-size neutrally buoyant particles in a channel. The governing equations, numerical method and computational set-up are presented in § 2. In § 3, we examine the dominant contributions to the drag in the newly established stress balance and the modifications to the turbulence. In § 4, the focus is directed to the differences in particle dynamics and microstructure between the Newtonian and viscoelastic conditions. Concluding remarks are presented in § 5.

2. Governing equations and simulation set-up

Throughout this work, all quantities are non-dimensional unless distinguished by a 'star' symbol. For incompressible viscoelastic flows laden with monodisperse spherical particles, five relevant non-dimensional parameters are defined: (i) the Reynolds number $Re = U^* \mathcal{L}^* / \nu^*$, where ν^* is the fluid total kinematic viscosity and U^* and \mathcal{L}^* are the characteristic velocity and length of the system; (ii) the Weissenberg number $Wi = \lambda^* U^* / \mathcal{L}^*$, which is the ratio of the viscoelastic fluid relaxation time λ^* to the flow time scale \mathcal{L}^* / U^* ; (iii) the density ratio of the dispersed and fluid phases, $\rho = \rho_p^* / \rho_f^*$, which is unity in the present case of neutrally buoyant particles; (iv) the ratio of the particle diameter to the characteristic length scale of the flow, $d_p = d_p^* / \mathcal{L}^*$; and (v) the bulk solid volume fraction of the system, $\varphi = N_p \mathcal{V}_p^* / \mathcal{V}_t^*$, where N_p , \mathcal{V}_p^* and \mathcal{V}_t^* denote the total number of particles, volume of a particle and the total volume of the computational domain.

2.1. Governing equations

The Navier–Stokes equations for a dilute polymer solution are,

$$\nabla \cdot \mathbf{u}_f = 0, \quad (2.1)$$

$$\frac{\partial \mathbf{u}_f}{\partial t} + \mathbf{u}_f \cdot \nabla \mathbf{u}_f = -\nabla p + \frac{\beta}{Re} \nabla^2 \mathbf{u}_f + \frac{(1-\beta)}{Re} \nabla \cdot \mathbf{T} + \mathbf{F}, \quad (2.2)$$

where subscript ‘*f*’ identifies the fluid phase. The quantity $\beta \equiv \mu_s^*/(\mu_s^* + \mu_p^*)$ is the ratio of the solvent to the total viscosities, the latter defined as the sum of the solvent μ_s^* and polymer μ_p^* contributions. In addition to the viscoelastic stress tensor \mathbf{T} , a generic force field \mathbf{F} is also included in (2.2). The viscoelastic stress is expressed in terms of the polymer conformation tensor \mathbf{c} , and using the FENE-P model,

$$\frac{\partial \mathbf{c}}{\partial t} + \mathbf{u}_f \cdot \nabla \mathbf{c} = \mathbf{c} \cdot \nabla \mathbf{u}_f + (\mathbf{c} \cdot \nabla \mathbf{u}_f)^T - \mathbf{T}, \quad (2.3)$$

$$\mathbf{T} = \frac{1}{Wi} \left(\frac{\mathbf{c}}{\psi} - \frac{\mathbf{I}}{a} \right); \quad \psi = 1 - \frac{\text{tr}(\mathbf{c})}{L_{max}^2}; \quad a = 1 - \frac{3}{L_{max}^2}, \quad (2.4)$$

where L_{max} is the maximum extensibility of the polymer chains and \mathbf{I} refers to the unit tensor.

Particles are assumed to undergo rigid-body motion, and therefore no-slip boundary conditions are imposed at their surfaces $\partial \mathcal{V}_p$,

$$\mathbf{u}_f|_{\partial \mathcal{V}_p} = \mathbf{u}_p + \boldsymbol{\omega}_p \times \mathbf{r}, \quad (2.5)$$

where \mathbf{u}_p and $\boldsymbol{\omega}_p$ are the particle translational and angular velocities, and \mathbf{r} is the distance vector emanating from the centre of the sphere. The motion of the particles is governed by the Newton–Euler Lagrangian equations,

$$\rho \mathcal{V}_p \frac{d\mathbf{u}_p}{dt} = \oint_{\partial \mathcal{V}_p} \boldsymbol{\sigma}_f \cdot \mathbf{n} dA + \mathbf{F}_c, \quad (2.6)$$

$$\rho \mathcal{I}_p \frac{d\boldsymbol{\omega}_p}{dt} = \oint_{\partial \mathcal{V}_p} \mathbf{r} \times \boldsymbol{\sigma}_f \cdot \mathbf{n} dA, \quad (2.7)$$

$$\boldsymbol{\sigma}_f = \frac{\beta}{Re} [-p\mathbf{I} + 2\mathbf{E}] + \frac{1-\beta}{Re} \mathbf{T}, \quad (2.8)$$

where $\mathcal{I}_p = \pi d_p^5/60$ and $\mathcal{V}_p = \pi d_p^3/6$ are the moment of inertia and the volume of a spherical particle, while $\boldsymbol{\sigma}_f$ is the fluid phase stress tensor. The force \mathbf{F}_c results from particle–particle or particle–wall collisions and \mathbf{n} is the outward unit vector at the particle surface. Lastly, \mathbf{E} is the strain-rate tensor of the fluid phase.

2.2. Numerical methodology

The solution of (2.1) and (2.2) is obtained numerically using a control-volume formulation and a fractional-step algorithm (Rosenfeld, Kwak & Vinokur 1991). The advection terms are treated explicitly using an Adams–Bashforth scheme, while an implicit Crank–Nicolson scheme is adopted for the treatment of the diffusion term and polymer stress.

The algorithm for the numerical solution of the conformation-tensor equations (2.3) was adopted in a number of high-fidelity simulations of instability waves and transition (Lee & Zaki 2017; Hameduddin, Gayme & Zaki 2019) as well as fully turbulent flows (Hameduddin *et al.* 2018; Hameduddin & Zaki 2019). The equations are marched in time using a third-order accurate Runge–Kutta method where the advection and polymer stretch terms are treated using an Adams–Bashforth

discretization within each sub-step. A semi-implicit method is adopted for the relaxation term, as suggested by Dubief *et al.* (2005). A variant of slope-limiting approach for spatial derivatives proposed by Vaithianathan *et al.* (2006) is used to ensure numerical stability without introducing any artificial diffusion. In brief, the advection term is evaluated using second-order accurate central difference scheme as long as the conformation tensor remains positive definite; when its smallest eigenvalue approaches zero, the discretization is replaced by the one-sided difference which maximizes the minimum eigenvalue (for details, see appendix B by Hameduddin *et al.* 2018).

The no-slip boundary conditions at the particle surfaces are enforced using a variant of the sharp-interface, robust immersed boundary (IB) method described by Nicolaou, Jung & Zaki (2015). The method was adapted for freely moving particles in viscoelastic fluids and the algorithm was optimized to take advantage of the geometric simplicity of the particles for computational efficiency. The IB force is included on the right-hand side of (2.2), $\mathbf{F} = \mathbf{F}^{IB}$, in order to satisfy the no-slip conditions (2.5). By integrating (2.2) over the volume of a particle and using the divergence theorem, the surface integral in (2.6) can be replaced by the volume integral (appendix B in Uhlmann 2005),

$$\rho \mathcal{V}_p \frac{d\mathbf{u}_p}{dt} = - \int_{\mathcal{V}_p} \mathbf{F}^{IB} d\mathcal{V}_p + \frac{d}{dt} \left(\int_{\mathcal{V}_p} \mathbf{u}_f d\mathcal{V}_p \right) + \mathbf{F}_c; \quad (2.9)$$

similarly, (2.7) can be rewritten as,

$$\rho \mathcal{I}_p \frac{d\boldsymbol{\omega}_p}{dt} = - \int_{\mathcal{V}_p} \mathbf{r} \times \mathbf{F}^{IB} d\mathcal{V}_p + \frac{d}{dt} \left(\int_{\mathcal{V}_p} \mathbf{r} \times \mathbf{u}_f d\mathcal{V}_p \right). \quad (2.10)$$

Following Breugem (2012), the second terms on the right-hand sides of equations (2.9) and (2.10) are evaluated over the fluid field occupying the solid domain. A short-range repulsive force proposed by Glowinski *et al.* (2001) is used to treat the particle–particle and particle–wall collisions and the conformation tensor is set to unity inside the solid domain.

Our numerical tool has been extensively validated in Newtonian turbulence (Lee *et al.* 2013), moving-body problems in Newtonian fluids (Nicolaou *et al.* 2015), and single-phase viscoelastic turbulence (Lee & Zaki 2017). In addition, we have verified the accuracy of our numerical tools in three reference configurations: a particle rotating in Newtonian and viscoelastic simple shear; lateral migration of an isolated particle in laminar Poiseuille flow; and Newtonian particle-laden turbulent flow in a channel. Details of these simulations are provided in appendix B.

2.3. Flow configuration

The computational domain is a channel geometry with the streamwise, spanwise and wall-normal directions aligned with x , z and y coordinates, as illustrated in figure 1. The bulk velocity U_b^* and channel half-height h^* are selected as the characteristic velocity ($\mathcal{U}^* = U_b^*$) and length ($\mathcal{L}^* = h^*$) for outer scaling. Where inner scaling is adopted, it is denoted by ‘+’ symbol and, unless otherwise stated, is defined based on the friction velocity $u_\tau^* \equiv \sqrt{\langle \tau_{wall}^* / \rho_f^* \rangle}$ and the length $l_\tau^* \equiv \nu^* / u_\tau^*$, where τ_{wall}^* is the total wall shear stress. The flow is maintained at constant mass flux, no-slip boundary

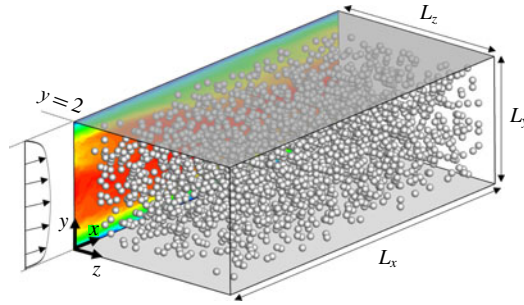


FIGURE 1. (Colour online) Schematic of the particle-laden simulations. No-slip boundary conditions $\mathbf{u}_f = 0$ are imposed at $y = \{0, 2\}$, and periodicity is enforced in the x and z directions.

Re	β, L_{max}	Wi	φ (%)	N_p	$1/d_p$	$L_x \times L_y \times L_z$	$N_x \times N_y \times N_z$	Case	Symbol
	Newtonian	0	0	0	—	$6 \times 2 \times 3$	$96 \times 192 \times 80$	W0	—
			5	2504	9	$6 \times 2 \times 3$	$864 \times 288 \times 432$	W0P5	⊖
2800	FENE-P	15	0	0	—	$10 \times 2 \times 4.5$	$160 \times 192 \times 120$	W15	—
			5	2504	9	$6 \times 2 \times 3$	$864 \times 288 \times 432$	W15P5	⊖
	$\beta = 0.97$	25	0	0	—	$10 \times 2 \times 4.5$	$160 \times 192 \times 120$	W25	—
	$L_{max} = 70$		5	2504	9	$6 \times 2 \times 3$	$864 \times 288 \times 432$	W25P5	⊖

TABLE 1. Physical and computational parameters of the simulations. Reynolds number $Re = h^* U_b^* / \nu^*$ and Weissenberg number $Wi = \lambda^* U_b^* / h^*$ are based on the channel half-height h^* , the bulk velocity U_b^* , total kinematic viscosity ν^* and viscoelastic fluid relaxation time λ^* . The domain sizes are $L_{\{x,y,z\}}$ in the $\{x, y, z\}$ directions, and the number of grid cells is $N_{\{x,y,z\}}$. The noted line types and symbols are adopted in figures, unless otherwise stated.

conditions are imposed at the bottom and top walls $y = \{0, 2\}$, and periodicity is enforced in the two horizontal directions.

Physical and computational parameters of the simulations are provided in table 1. One Newtonian and two viscoelastic conditions are simulated, each with and without the presence of neutrally buoyant spherical particles. A designation is introduced in table 1 to identify each simulation: letter W is followed by the Weissenberg number Wi and P by the bulk solid volume fraction of the system φ (%) in the associated case. In all simulations the grid cells are uniformly distributed in the streamwise and spanwise directions. In the wall-normal direction, the grid spacing is uniform in the particle-laden conditions and a hyperbolic tangent grid stretching is adopted in the single-phase simulations. In the particle-laden flows, the grid size is dictated by the required number of grid cells to correctly predict the flow field in the vicinity of the particles. Following previous studies (Goyal & Derksen 2012; Picano *et al.* 2015), the ratio of particle diameter to the grid cell size is set to $d_p / \Delta x = 16$.

The single-phase Newtonian simulation is initialized using a superposition of laminar Poiseuille flow and small-amplitude random fluctuations which trigger breakdown to turbulence, while turbulence is triggered in the particle-laden case naturally due to the presence of the randomly seeded particles. The viscoelastic conditions are initialized with the velocity and pressure fields from their Newtonian

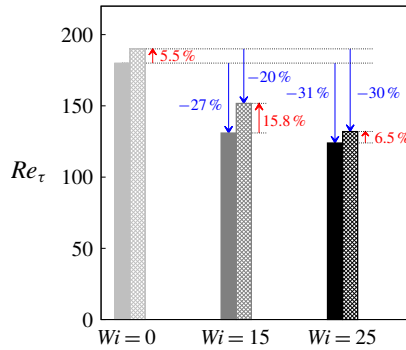


FIGURE 2. (Colour online) Friction Reynolds number Re_τ . Solid columns are single-phase conditions and hashed columns are particle-laden cases.

counterparts in the statistically stationary state. Beyond the initial transients, ensemble-averaged statistics of any mixture quantity $\langle o \rangle$ were evaluated, conditioned on the fluid and particle phases, and denoted $\langle o_{\{f,p\}} \rangle_{\{f,p\}}$. The unconditional average can be reconstructed,

$$\langle o \rangle = \langle (1 - \chi)o_f \rangle + \langle \chi o_p \rangle = (1 - \phi)\langle o_f \rangle_f + \phi\langle o_p \rangle_p, \tag{2.11}$$

where $\chi = \{0, 1\}$ is a phase indicator of the fluid and solid, and $\phi = \langle \chi \rangle$ is the solid volume fraction. Averaging is performed in the homogeneous streamwise and spanwise directions, as well as in time. Note that the subscripts $\langle \bullet \rangle_{\{f,p\}}$ are henceforth dropped and conditional averaging is implied. Fluctuations in any fluid or particle quantities are defined relative to their respective means, $o'_{\{f,p\}} = o_{\{f,p\}} - \langle o_{\{f,p\}} \rangle$. Statistics were collected for sufficiently long periods (e.g. 1800 convective times for case W15P5) in order to ensure convergence which was verified by comparing results from half and the total number of samples.

3. Stress balance and turbulence modifications

3.1. Drag modulation and stress budget

The friction Reynolds number $Re_\tau \equiv Re u^*_b / U^*_b$ is reported in figure 2. Particle-laden cases systematically experience higher Re_τ relative to their single-phase counterparts. A similar trend was observed in previous studies of Newtonian flows laden with dilute and dense suspensions of spherical particles (Picano *et al.* 2015; Lashgari *et al.* 2016; Costa *et al.* 2018). Those studies generally concur that the particle stress is responsible for the drag enhancement. A curious observation from figure 2 is that the particle drag enhancement is higher in the low Weissenberg case (15.8% for W15P5), in comparison to both the Newtonian (5.5% for W0P5) and high Weissenberg (6.5% for W25P5) cases. In addition, the effectiveness of the polymer to reduce drag in the low Weissenberg particle-laden case is appreciably diminished in the particle laden case, $Re_\tau^{W15} / Re_\tau^{W0} < Re_\tau^{W15P5} / Re_\tau^{W0P5}$. At the high Weissenberg condition, however, the propensity of viscoelasticity to reduce drag appears largely unaffected by the presence of the particle phase.

The above observations will be examined in detail and explained, starting by an assessment of the different contributions to the total stress τ_{tot} at every wall-normal

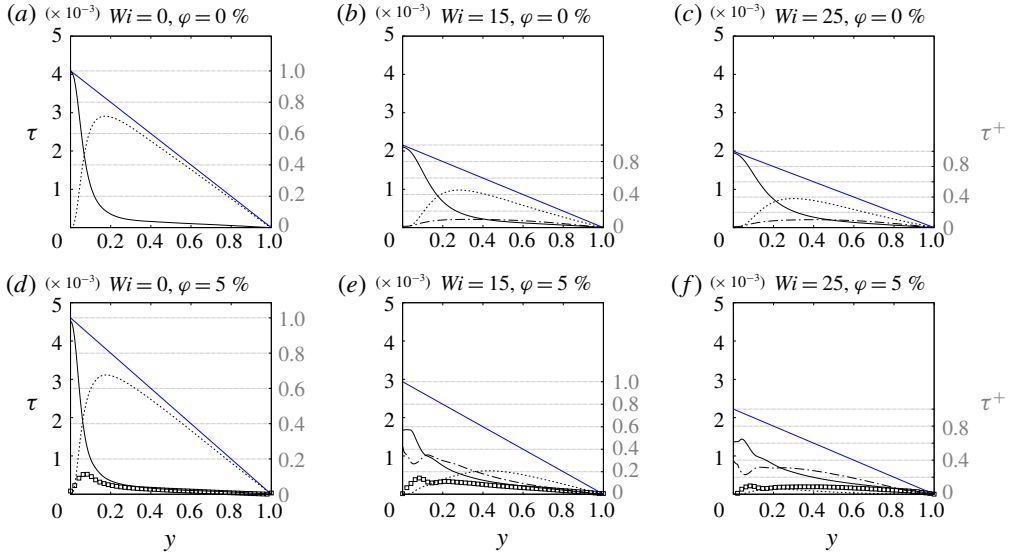


FIGURE 3. (Colour online) Wall-normal profiles of the stresses defined in (3.1): blue solid lines (—) total stress τ_{tot} ; black solid lines (—) viscous stress τ_μ ; dotted lines (.....) turbulent Reynolds stress τ_{Re} ; dash-dotted lines (-.-.) polymer stress τ_β ; square symbols (\square) particle-induced stress τ_ϕ . The stresses are plotted in (left axes) outer and (right axes) wall units.

position,

$$\begin{aligned}
 & \underbrace{-[(1 - \phi)\langle u'_f v'_f \rangle + \phi\langle u'_p v'_p \rangle]}_{\tau_{Re}} + \underbrace{\frac{\beta}{Re}(1 - \phi)}_{\tau_\mu} \frac{d\langle u_f \rangle}{dy} \\
 & + \underbrace{\frac{(1 - \beta)}{Re}(1 - \phi)\langle T_{xy} \rangle}_{\tau_\beta} + \underbrace{\phi\langle \sigma_{p,xy} \rangle}_{\tau_\phi} = \underbrace{\langle \tau_{wall} \rangle}_{\tau_{tot}}(1 - y). \tag{3.1}
 \end{aligned}$$

From left to right, these contributions are the turbulent Reynolds stress τ_{Re} , the viscous stress τ_μ , the polymer stress τ_β and the particle stress τ_ϕ . Figure 3 compares the contribution of each term for different cases in outer (left axis) and inner (right axis) scaling. As anticipated for the single-phase viscoelastic flows, τ_{Re} is significantly attenuated and the incurred viscoelastic stress τ_β is relatively small (figures 3(a), 3(b) and 3(c)); the net effect is a decrease of the total stress. The addition of particles to the Newtonian fluid leads to an induced stress which plays a major role in drag enhancement, while the share of turbulent Reynolds stress is almost unchanged relative to W0. In contrast, the addition of particles appreciably reduces the contribution of τ_{Re} to the total stress in the viscoelastic cases – an effect that may seem counter-intuitive at first given that the total drag has increased in W15P5 and W25P5 relative to W15 and W25. The drastic increase in the polymer stresses explains the overall increase in drag in the presence of the particles. In cases W15P5 and W25P5, τ_β is comparable to the viscous stress contribution near the wall and takes a significant share of the total stress throughout the channel. On balance, the attenuation of the turbulence

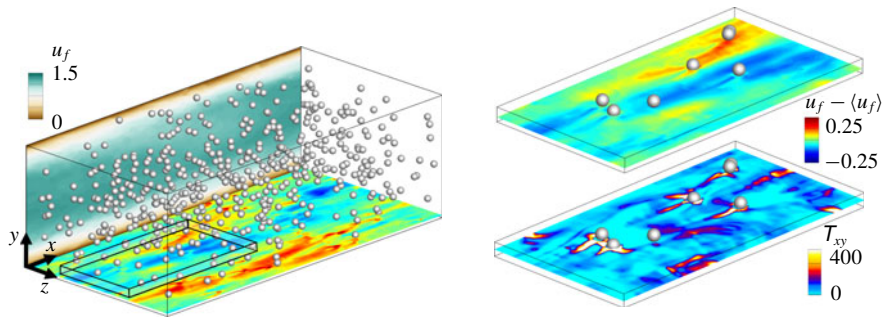


FIGURE 4. (Colour online) Instantaneous snapshot of particle positions, contours of u_f (vertical plane) and $u_f - \langle u_f \rangle$ (horizontal plane) for case W15P5. For clarity, only 20% of particles are shown. Marked area is magnified and reproduced with contours of T_{xy} .

shear stress and the polymer stress enhancement in the vicinity of the particles result in a less effective drag reduction in case W15P5 relative to W15, and an almost equal level of drag reduction in cases W25P5 and W25.

The pronounced increase of polymer stress in the particle-laden viscoelastic configurations arises due to the polymer stretching mechanism which differs from the single-phase flow. In the latter, polymer chains are stretched by the turbulent fluctuations. In the two-phase configuration, particles alter the velocity field in their vicinity and cause local stretching of polymer chains and enhancement of the associated stresses (figure 4); this effect is examined in detail in § 4.1.

The turbulent stresses τ_{Re} in the reference cases W15 and W25 are within 25% of one another. And while the addition of the particle phase reduces τ_{Re} at both elasticities, it is much more influential at the higher Weissenberg number: W15P5 experiences a twofold reduction compared to fourfold in case W25P5. This prominent dissimilarity is a sign of intrinsic differences in particle–turbulence interactions in W15P5 and W25P5, and calls for further scrutiny of the time-dependent effects that contribute to this average stress (§ 3.3). Lastly, in all particle-laden cases, a peak in the particle stress is recorded near $y = 0.1$, approximately one diameter from the wall, where the particles are expected to experience high relative velocity with respect to the fluid. However, the contribution of the particle stress is more evenly distributed throughout the channel in cases W15P5 and W25P5, relative to the Newtonian W0P5 where it is most relevant in the near-wall region. The persistent contribution in the outer flow in the viscoelastic cases reinforces a potential change in the role of particles in the wall-normal momentum transport.

3.2. Mean fluid velocity and Reynolds stress profiles

The mean streamwise fluid velocity profiles are reported in figure 5, in outer and inner scaling. The characteristic velocity for the latter scaling is based on the viscous component of the wall shear stress, i.e. $u_\mu^* \equiv \sqrt{\langle \tau_{\mu,wall}^* / \rho_f^* \rangle}$. In the viscoelastic cases, $\langle u_f \rangle$ deviates from the Newtonian turbulent channel-flow profile and approaches the laminar solution. The deviation from the Newtonian turbulent profile is a signature of suppressed wall-ward momentum mixing. As described by White *et al.* (2018), polymer stress takes over the role of Reynolds stress with respect to inertial mixing, but is less effective; a reduced level of momentum mixing in the wall-normal direction eventually results in the modification of the law of the wall. The addition

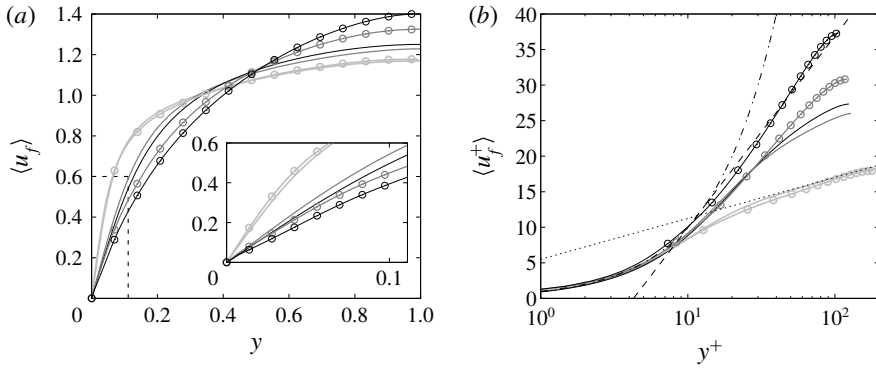


FIGURE 5. Mean streamwise fluid velocity in (a) outer and (b) inner units. Line types as listed in table 1: (—) W0; (—) W15; (—) W25; (—○) W0P5; (—○) W15P5; (—○) W25P5. (a) Marked area is magnified in the inset. (b) Dashed line (---) is the Virk asymptote (Virk *et al.* 1970); dotted line (.....) Newtonian law of the wall $\langle u_f^+ \rangle = 2.5 \log(y^+) + 5.0$; dashed dotted line (-.-.) laminar Poiseuille profile $\langle u_f^+ \rangle = y^+$.

of particles intensifies this effect to the point where the profile from W25P5 tends to Virk's maximum drag reduction asymptote (Virk *et al.* 1970). This shift can be an indication that the particles effectively suppress the turbulent fluctuations and, in turn, the associated momentum mixing. Nevertheless, the impact of particles on the mean streamwise velocity profile is almost negligible in W0P5. Previous studies have shown that in semi-dilute particle-laden Newtonian flows, except in the near-wall region, particles render the mean streamwise velocity profile similar to the laminar case (Picano *et al.* 2015; Costa *et al.* 2018). In the near-wall region, however, particles are known to accelerate the fluid velocity due to their finite slip (Shao *et al.* 2012). This effect is weakly apparent in case W0P5 and overshadowed by the strong modification of the mean streamwise velocity profile due to the turbulence attenuation in cases W15P5 and W25P5 (inset of figure 5(a)).

The impact of the particle phase on the turbulence fluctuations is captured by the Reynolds stresses (figure 6). First recall that viscoelasticity alone is known to swell the streamwise streaks thus resulting in an upward shift of the peak of streamwise fluctuations; in addition, relative to Newtonian flows, the peak value of the streamwise stress increases at low/moderate elasticity and reduces at high elasticity (Dallas *et al.* 2010; Xi & Graham 2012). Figure 6(a) shows that the peak streamwise stresses for W15 and W25 shift away from the wall, without any significant change in its value. Particles weaken the streamwise vortices and decrease the peak streamwise velocity fluctuations in the Newtonian and viscoelastic cases. This effect, associated with the particle slip velocity acting as a sink of kinetic energy in the coherent streaks, is substantially intensified in the viscoelastic flows. For the wall-normal and spanwise stresses, however, the picture is quite divergent. In the near-wall region, where the particles are the main source of cross-flow fluctuations due to their finite slip velocity, $\langle v_f'v_f' \rangle$ and $\langle w_f'w_f' \rangle$ are higher in all particle-laden cases relative to the single-phase counterparts. However, qualitative differences in the impact of particles on the Newtonian and viscoelastic flows arise away from the wall: while in W0P5, particles slightly enhance the cross-stream fluctuations, in W15P5 and W25P5 they attenuate the fluctuations in most of the channel. In the Newtonian case, the particles redistribute momentum from the streaks to the cross-stream directions by inducing particle-scale vortices (Shao *et al.* 2012). Since the streaks are appreciably weakened

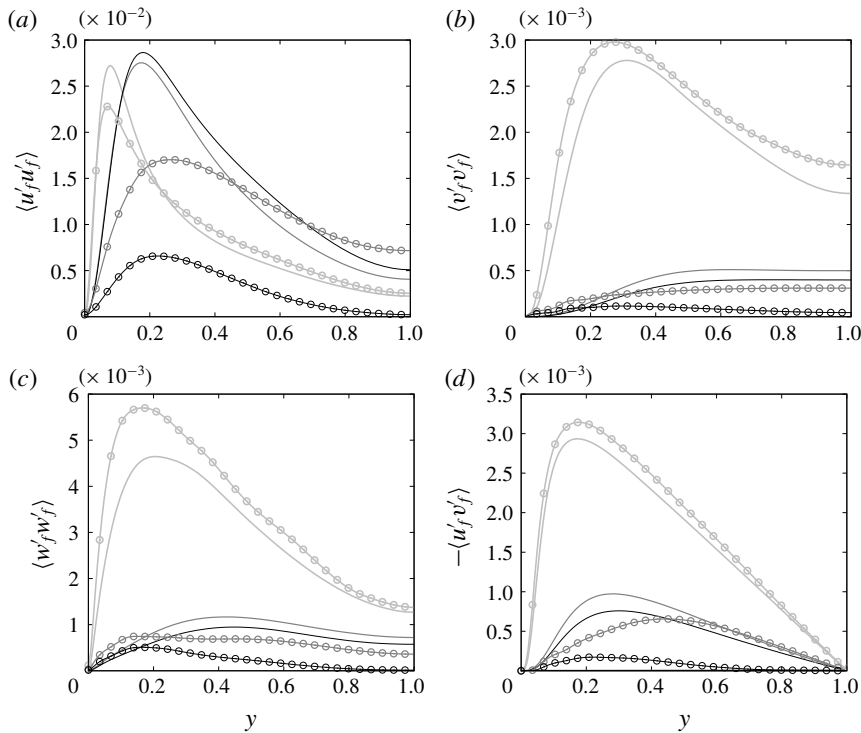


FIGURE 6. Components of the Reynolds stress tensor, where u'_f , v'_f and w'_f are the fluctuations in the streamwise, wall-normal and spanwise fluid velocities. Line types as listed in table 1: (—) W0; (—) W15; (—) W25; (—○) W0P5; (—○) W15P5; (—○) W25P5.

in viscoelastic flows and, as a result, this effect is muted in W15P5 and W25P5, the cross-stream fluctuations are also reduced. Moreover, in contrast to the Newtonian case the presence of particles in viscoelastic flows reduces, rather than enhances, the turbulent shear stress – a matter that we examine in detail in § 3.3.

3.3. Transient dynamics and conditional statistics

The regeneration cycle of wall turbulence involves (i) formation of streamwise-elongated streaks, (ii) breakdown of the streaks and (iii) generation of streamwise vortices which enhance the three-dimensionality of the flow and are followed by a surge in the wall shear rates. In Newtonian fluids, particles reinforce the generation of streamwise vortices and promote the wall shear stress (Wang, Abbas & Climent 2018). On the other hand, viscoelasticity alters the cycle by promoting extended periods of low shear rates known as ‘hibernating’ states, which sporadically give way to bursts of high shear-rate ‘active’ states of turbulence. Xi & Graham (2012) showed that once viscoelasticity surpasses a critical value, the stretching of polymer chains weakens the turbulent fluctuations and in turn contributes to the dominance of the hibernating state. Due to the lower shear stress associated with hibernating turbulence, polymer solutions experience a lower turbulent drag in an average sense. In an effort to determine the influence of the particle phase on this process, we examine the transient dynamics in our simulations within a similar framework.

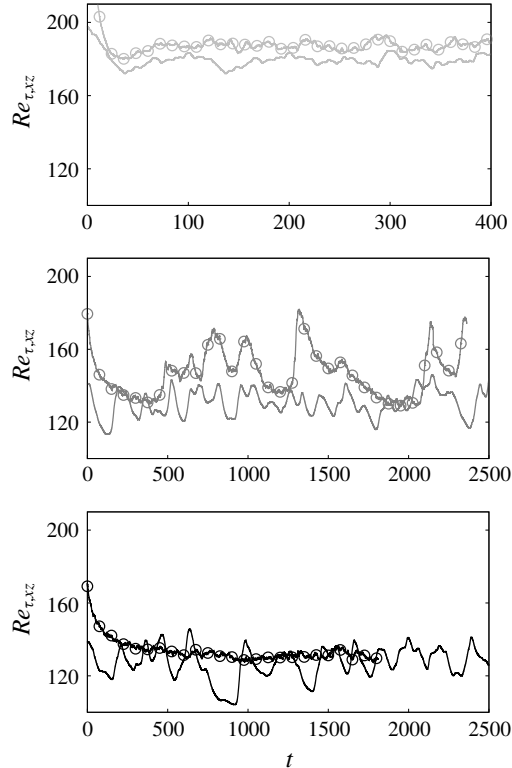


FIGURE 7. Time series of $Re_{\tau,xz}$. Line types as listed in table 1: (—) W0; (—) W15; (—) W25; (—○) W0P5; (—○) W15P5; (—○) W25P5.

Figure 7 contrasts the time evolutions of the wall-averaged instantaneous friction Reynolds numbers, $Re_{\tau,xz} \equiv Re \sqrt{(1/\rho_f^*) \langle \tau_{wall}^* \rangle_{xz} / U_b^*}$, from the different simulations. In both Newtonian flows, W0 and W0P5, very minimal fluctuations are observed which is indicative of an active turbulence state. While the hibernating state also exists in Newtonian flows (Xi & Graham 2010), it is relatively rare and its influence is overshadowed by the strong dominance of active turbulence. In the low Weissenberg cases, W15 and W15P5, the fluctuating behaviour of $Re_{\tau,xz}$ signals a competition between active and hibernating states. Infrequent peaks of $Re_{\tau,xz}$ in W15P5 indicate that the hibernating state prevails. At high Weissenberg, W25 demonstrates a cyclic behaviour akin to that of W15, but W25P5 appears dominated by the hibernating state. In both W15P5 and W25P5, the particles complement the influence of viscoelasticity by promoting hibernation, or suppressing active turbulence. The drag itself is, nonetheless, increased in presence of the particles due to the increase in the polymer stress, as noted in § 3.1.

The mean streamwise velocity profiles were evaluated conditioned on the state of the turbulence, and the hibernating and active states are contrasted to the conventional mean in figure 8, for W15 and W15P5. In line with the observations by Wang, Shekar & Graham (2017), at both Weissenberg numbers the profile of the hibernating state is closer to Virk's asymptote, and that of active turbulence is closer to Newtonian turbulence. In W15P5, the overall average is biased towards the hibernating state-conditioned profile, in agreement with the scarcity of the active

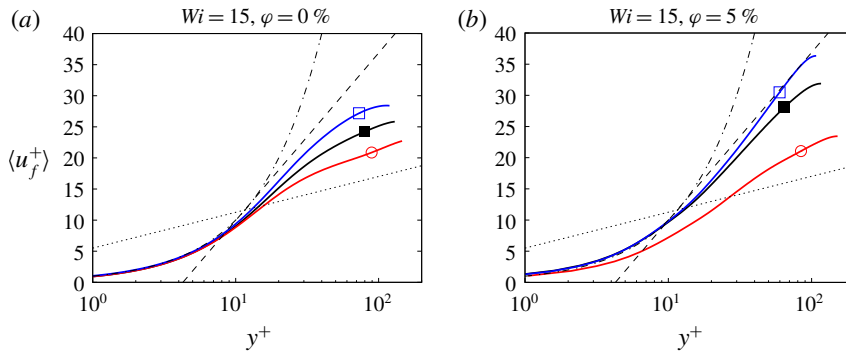


FIGURE 8. (Colour online) Wall-normal profiles of the overall and conditional averages of streamwise velocity for (a) W15 and (b) W15P5. Averages are computed over the homogeneous streamwise and spanwise directions and (black lines, ■) the full sampling time, (blue lines, □) hibernating states and (red lines, ○) active states. Each curve is normalized by its respective u_{μ}^* .

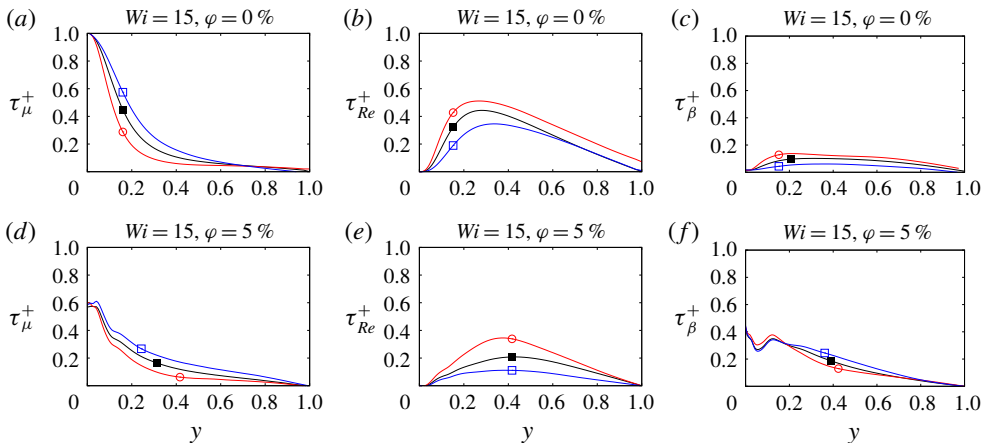


FIGURE 9. (Colour online) Wall-normal profiles of the overall and conditional averages of contributions to the shear stress (3.1). Averages are computed over the homogeneous streamwise and spanwise directions and (black lines, ■) the full sampling time, (blue lines, □) hibernating states and (red lines, ○) active states. (a–c) case W15; (d–f) case W15P5.

turbulence instances in figure 7. Figure 9 compares different components of the stress budget during the hibernating and active turbulence states, for W15 and W15P5. Without and with particles, during the hibernating state the Reynolds stress τ_{Re} is reduced and the viscous stress τ_{μ} increased. Similar to previous studies of single-phase viscoelastic turbulence (Xi & Graham 2010; Tamano, Graham & Morinishi 2011; Wang *et al.* 2017), the share of the polymer stress in W15 increases during the active state. The effect has been interpreted in terms of the polymer chains being stretched and relaxed during the active and hibernating states, respectively, giving rise to the similar trend in polymer and turbulent stresses (Wang *et al.* 2017). Interestingly, however, τ_{β} exhibits the opposite behaviour in W15P5: in most of the channel the contribution of the polymer stress is slightly higher during the hibernating state

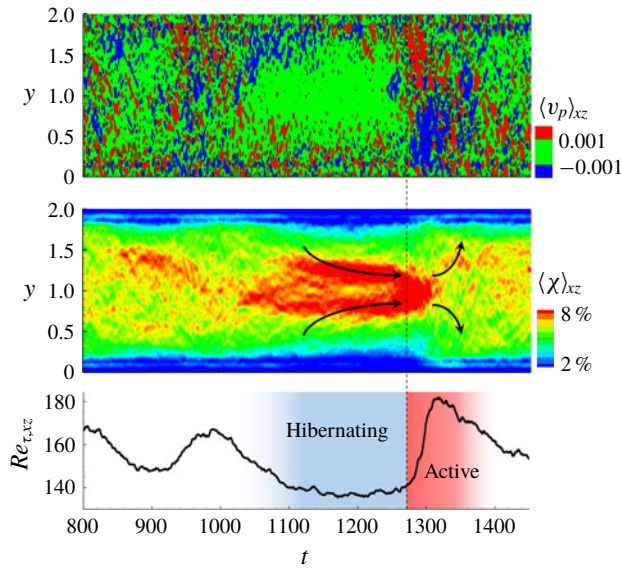


FIGURE 10. (Colour online) Particle migration during the hibernating and active turbulence states in case W15P5. Time evolution of contours of streamwise- and spanwise-averaged (top) particle wall-normal velocity, (middle) phase indicator and (bottom) $Re_{\tau,xz}$.

relative to the active one. This change in character will be ascribed to the presence of particles, which will be demonstrated in §4.1 to be the primary cause of polymer stretch. In other words, τ_β in W15P5 is inherently different from its single-phase counterpart.

The importance of the particle phase becomes evident when their behaviour is examined as the turbulence shifts from the hibernating to active state. Figure 10 shows the time dependence of the spatially averaged particle velocity $\langle v_p \rangle_{x,z}$ and phase indicator $\langle \chi \rangle_{x,z}$ during this shift. Particles gradually migrate towards the channel centre during the hibernating state. Due to the subdued turbulence activity, momentum mixing is weak and the mean streamwise velocity tends towards the parabolic profile. As a result, the particles' migration towards the channel centre is similar in nature to their lateral migration in laminar viscoelastic Poiseuille flow (see e.g. Huang *et al.* 1997; Li, McKinley & Ardekani 2015, and appendix B). As they migrate to the centre, their streamwise velocity will increase due to the higher local momentum; however their fluctuating motion is attenuated during the hibernating state due to the weaker turbulence activity. Migration towards the channel centre continues until the near-wall region is almost devoid of particles, $\langle \chi \rangle_{xz} < 2\%$. At this stage, active turbulence is reinitiated and the particles are pushed back towards the wall by the fluctuating motions. As a result, the streamwise fluid velocity profile is flattened by turbulent mixing, and particle fluctuations are once again revived.

Particle migration is key to understanding the increased contribution of the polymer stress during hibernation (figure 9(f)). Upon closer examination of figures 9(f) and 10, we observe that this increase takes place only where the particles are more concentrated, i.e. in the outer region ($y > 0.2$) during hibernation. In fact, near the wall, the contribution of the polymer stress is larger during the active state due to the coexistence of turbulence-induced polymer stretch and the return of the particles towards the wall as the turbulence is revived.

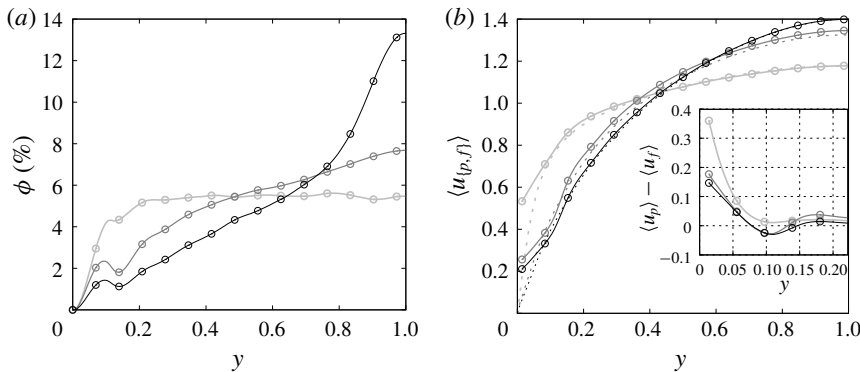


FIGURE 11. Wall-normal profiles of (a) solid volume fraction and (b) mean streamwise particle and fluid velocities. Line types as listed in table 1: (—○) W0P5; (—○) W15P5; (—○) W25P5. (b) Dashed lines correspond to the fluid velocities; Inset shows the mean relative particle velocities.

4. Particle dynamics and microstructure

4.1. Particle dynamics

The focus is now placed on the particle dynamics, and its connection to the Newtonian and viscoelastic flow statistics. The solid volume fraction profiles are reported in figure 11(a). In the Newtonian case, a flat profile in the outer region signals an even distribution of particles, due to strong turbulent mixing. In viscoelastic conditions, the solid volume fraction increases away from the wall, and at the channel centre of case W25P5 exceeds twice its bulk value ($\phi = 5\%$). This finding is in line with the particle migration mechanism explained in §3.3. Note that this migration behaviour is due to fluid elasticity. It is therefore inherently different from the phenomenologically similar migration towards the channel centre that can take place in Newtonian turbulence, at high solid volume fractions $\phi \geq 30\%$ or density ratios $\rho_p^*/\rho_f^* \approx 10$ (Fornari *et al.* 2016; Lashgari *et al.* 2016); that effect is due to a particle normal stress imbalance in the wall-normal direction. A stabilized layer of particles is formed near the wall in cases W15P5 and W25P5, and is due to the particle–wall lubrication effect and asymmetric interactions in that region. The same mechanism is present in Newtonian particle-laden flows at higher solid volume fractions (Yeo & Maxey 2011; Lashgari *et al.* 2016), and is observed here in the viscoelastic cases despite a highly dilute concentration of particles near the wall.

The mean streamwise particle and fluid velocity profiles are plotted in figure 11(b). In each case, the mean fluid and particle velocity profiles are in good agreement near the core of the channel; however, the particle streamwise velocity is larger than that of the fluid in close vicinity to the wall ($y \leq 0.5d_p$, $y^+ \leq 10$). A positive particle slip, loosely defined as the particle velocity relative to the local fluid velocity, is evident in the viscous sublayer and is due to the particles' finite rigid-body motion while the fluid velocity vanishes. Surprisingly, a negative slip velocity is observed near $0.75d_p \leq y \leq 1.5d_p$ in W15P5 and W25P5 (inset of figure 11(b)). Its interpretation must, however, be carefully considered in light of the heterogeneity of the particle distribution which can introduce bias if the simple definition of slip as $\langle u_p \rangle - \langle u_f \rangle$ is adopted.

A more precise definition of the velocity experienced, or seen, by the particles is required in order to estimate the slip velocity. We adopt the definition proposed by Kidanemariam *et al.* (2013): the instantaneous fluid velocity is integrated over a

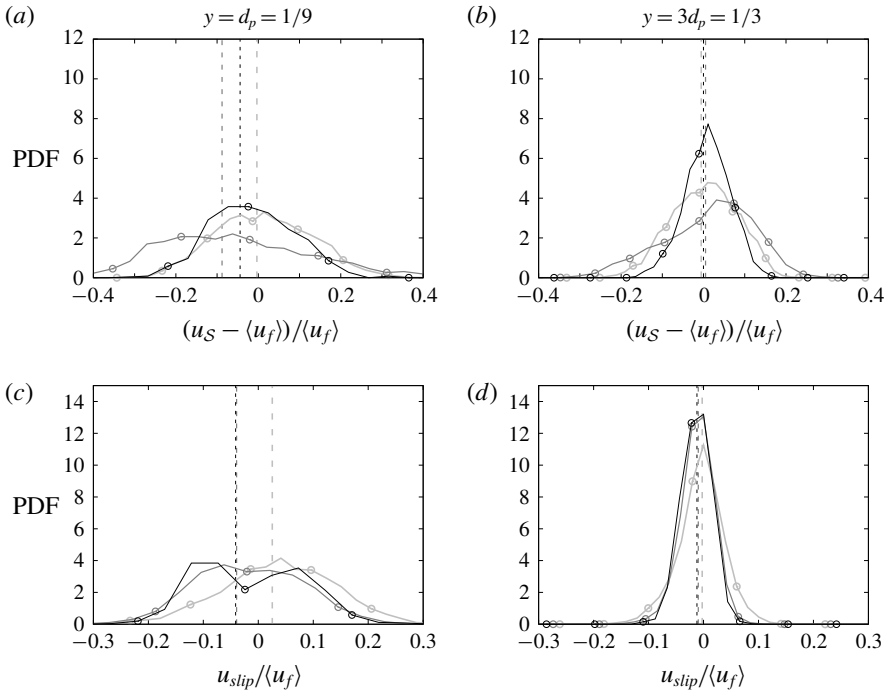


FIGURE 12. Probability density function (PDF) of normalized (a,b) perturbation shell velocity and (c,d) slip velocity. The median of each PDF is marked by a vertical dashed line. Line types as listed in table 1: (—○) W0P5; (—○) W15P5; (—○) W25P5. The shell and slip velocities are defined in (4.1) and (4.2). Data are conditionally sampled for particles at (a,c) $y = 1/9$ and (b,d) $y = 1/3$.

spherical shell, \mathcal{S} , with diameter equal to $3d_p$ and centred around the particle. In order to avoid sampling bias due to heterogeneity in y , the shell surface is trimmed by two wall-parallel planes located at one radius below and above the particle position. Formally, the shell and particle slip velocities are defined as,

$$u_S = \frac{\oint_{\mathcal{S}} (1 - \chi) u_f \, dA}{\oint_{\mathcal{S}} (1 - \chi) \, dA}, \tag{4.1}$$

$$u_{slip} = u_p - u_S. \tag{4.2}$$

A shell perturbation velocity can be defined relative to the local mean fluid velocity, $u_S - \langle u_f \rangle$. Probability density functions (PDFs) of this quantity are reported in figure 12 at two heights from the wall, normalized by $\langle u_f \rangle$. According to figure 12(a), a wide range of positive and negative shell perturbation velocities are experienced by the particles in both the Newtonian and viscoelastic cases, and a slight bias towards negative values is present for the latter. This trend signals a preferential concentration of particles in low-speed streaks in the buffer layer ($15 \leq y^+ \leq 21$), which is precipitated by sweeping high-speed vortices that displace the particles into low-speed regions. This phenomenon has been reported for Newtonian wall turbulence, in the case of point particles (Kaftori *et al.* 1994; Pan & Banerjee 1997) and small

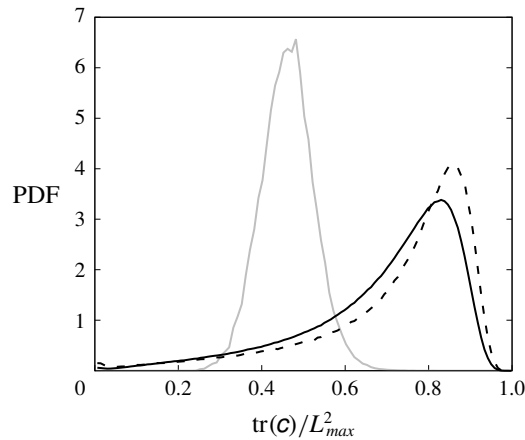


FIGURE 13. PDF of the normalized trace of the conformation tensor, sampled for fluid points at $y = 0.15$. Solid grey line (—): W15; black line (—): W15P5; black dashed line (---): sampled points are also constrained to be within a spherical region concentric with particles and twice their diameter in case W15P5.

particles with size $d_p^+ \approx 5\text{--}10$ (Kidanemariam *et al.* 2013; Wang *et al.* 2018), but has not been observed for large particles ($d^+ \approx 30$) (Hetsroni & Rozenblit 1994). Since turbulence structures, in particular streaks, are inflated by viscoelasticity and thickened in the enlarged buffer layer, the relative particle size is smaller than in the Newtonian configuration. As a result, the particles further adapt to the fluid motion induced by the near-wall streamwise vortices, preferentially residing in the low-speed streaks. In the log layer ($35 \leq y^+ \leq 63$), the distribution of normalized shell velocity perturbation is centred at zero and predictably narrowed (figure 12(b)), in both the Newtonian and viscoelastic cases.

Figure 12 also reports PDFs of the normalized slip velocity, which are also broad in the buffer layer and narrower in the log layer. In the former region (figure 12(c)), viscoelasticity enhances the probability of particles experiencing negative slip. Together figures 12(a) and 12(c) clarify that the negative relative mean velocities reported in figure 11(b) in the viscoelastic cases stem from the combination of two effects: (i) preferential location of particles in the low-speed streamwise velocity zones and (ii) mean negative slip velocity of particles with respect to their shell velocity. In the log layer (figure 12(d)), the PDFs of normalized slip velocity are centred at zero. Although narrow relative to their counterparts in the buffer region, the widths of all distributions are still non-negligible particularly when compared to the normalized turbulence fluctuations. Specifically, in all particle-laden cases the variance of $u_{slip}/\langle u_f \rangle$ is comparable in magnitude to $\sqrt{\langle u_f' u_f' \rangle} / \langle u_f \rangle$. This observation is notable for two reasons: (i) it shows that despite the zero average slip velocity, particles still act as effective sinks of kinetic energy in the log layer, which explains their significant role in the reduction of the fluid streamwise velocity fluctuations (figure 6); (ii) a non-zero slip velocity gives rise to the stretching of polymer chains in the neighbourhood of the particles.

In § 3.1, the pronounced increase of polymer stress in the presence of particles was ascribed to stretching of the polymer in their vicinity (figure 3). This assertion is supported by comparing the PDFs of the normalized trace of the conformation tensor, $\text{tr}(\mathbf{c})/L_{max}^2$, in cases W15 and W15P5 (figure 13). The comparison is made at

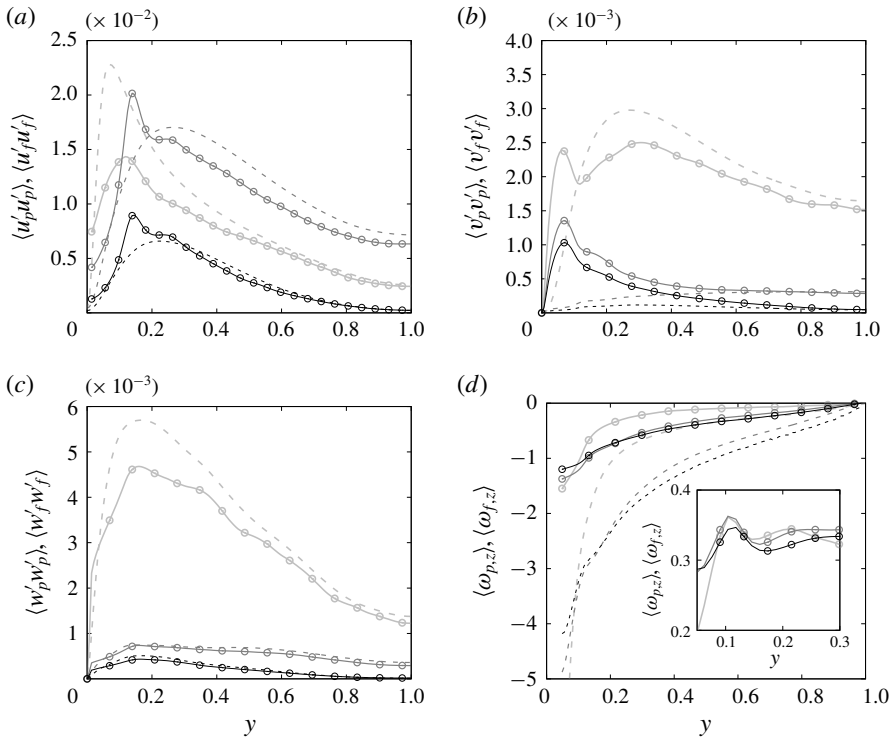


FIGURE 14. Comparison of particle and fluid velocity fluctuations in the (a) streamwise, (b) wall-normal and (c) spanwise directions. (d) Comparison of particle mean rotation in the spanwise direction and fluid vorticity; inset depicts the ratio of the two quantities in the near-wall region. Line types as listed in table 1: (—○) W0P5; (—○) W15P5; (—○) W25P5. Quantities in the fluid phase are represented by dashed lines.

$y = 0.15$, where the polymer stress contribution differs dramatically in the two cases (compare figures 3(b) and 3(e)). The evident dissimilarity between the shapes of the distributions in figures 13 highlights the qualitative difference in polymer stretching in the single-phase and particle-laden cases. In the absence of particles, the stretching of polymer chains, measured by the trace of the conformation tensor, has nearly a Gaussian distribution. In contrast, in the particle-laden case the distribution is highly skewed towards more stretched polymer chains. By exclusively considering fluid points located in the vicinity of the particles, specifically within spheres concentric with the particles and twice their diameter, the distribution is further skewed towards higher values, which points to the role of particles in the stretching of polymer chains.

Statistics of fluctuations in the particle and fluid velocities are plotted in figure 14; the fluid curves are reproduced from figure 6. In the streamwise direction, a non-monotonic behaviour is observed in the outer region: low viscoelasticity enhances the particle fluctuations beyond the Newtonian results but higher Weissenberg number reverses this effect and yields lower $\langle u_p' u_p' \rangle$ than Newtonian. This trend parallels the effect on fluid fluctuations, which was discussed in connection with figure 6: elasticity expands the turbulent structures thus shifting the peak $\langle u_f' u_f' \rangle$ towards the core of the channel, and ultimately attenuates the magnitude of turbulent fluctuations.

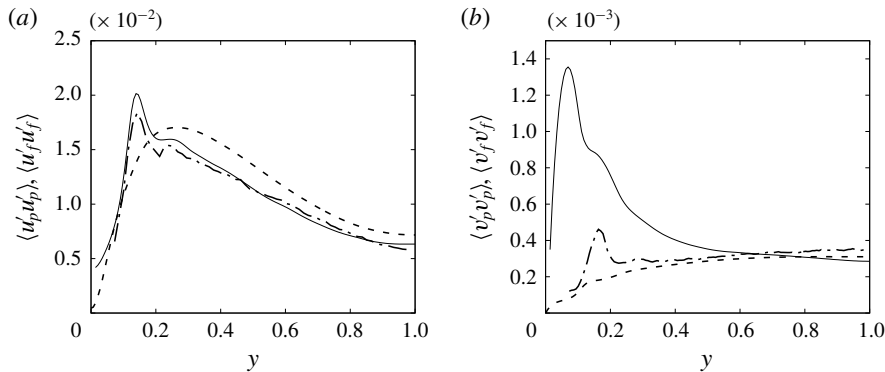


FIGURE 15. Particle fluctuations in (a) streamwise and (b) wall-normal directions in case W15P5. Particle averages were performed using (—) full rigid-body motion and (---) motion of particle centres only; (· · ·) fluid fluctuations.

In the Newtonian fluid, all three components of the particle fluctuations are lower than the fluid ones throughout most of the channel, and the trend reverses near the wall. For the streamwise and spanwise components the trend reverses in a very small near-wall layer, and for the wall-normal component the reversal appears at wall distances below one diameter. In contrast to the Newtonian case, in the viscoelastic fluids all three components of the particle velocity fluctuations are commensurate with or exceed the fluid ones. The streamwise component exceeds the fluid values over a thick near-wall region of similar size to the particle diameter; the wall-normal particle fluctuations are notably higher than the fluid ones over a large part of the channel; and the spanwise fluctuations are essentially equal to the fluid ones except in the close vicinity of the wall where the particle slip velocity is finite.

Since the mean vorticity vector is aligned with the spanwise coordinate, the particles sustain a mean angular velocity in that direction. The two quantities, namely the spanwise vorticity and particle angular velocity, are compared in figure 14(d). The impact of viscoelasticity on the vorticity distribution is also observed in the particle angular velocities, which are increased in the bulk of the channel relative to the Newtonian case. When normalized, $\langle \omega_{p,z} \rangle / \langle \omega_{f,z} \rangle$ is similar for all three cases within the region $y \leq 0.2$ (inset of figure 14(d)).

The particles' mean spanwise angular velocity strongly affects their velocity fluctuations in the x and y directions. This effect is isolated by comparing the velocity fluctuations of the particle centres to those of the particles in full rigid-body motion (figure 15); only case W15P5 is considered for brevity since the results are qualitatively similar to the other conditions. The effect of particles' rotation on their streamwise velocity fluctuations appears minimal (figure 15(a)). In the wall-normal component, however, the impact is much more pronounced: the fluctuations of the particle centres are at the same level as those in the fluid phase in most of the channel, and the large peak observed in the full rigid-body results near $y \approx 0.08$ nearly vanishes (figure 15(b)). Particle rotation thus plays an important role in establishing this peak when the full rigid-body motion is considered. In both the streamwise and wall-normal directions, the fluctuations of the particle centres have small local maxima near $y \approx 0.17$, which are due to the bouncing motion when particles with high inertia collide with the stabilized layer of particles close to the wall. This assertion is supported by a large peak in the profile of fluctuations in the

collision force at the same y position (not shown). Moreover, particles leaving the near-wall stabilized layer experience a rapid increase in their streamwise velocity, due to the large mean gradient in the region $0.1 \leq y \leq 0.2$ (see figure 11(b)), which accounts for the maximum in the fluctuations of the particle centres.

4.2. Particle clustering and microstructure analysis

Even in the simple case of two settling spheres in a quiescent flow, the attraction/repulsion of a particle pair in a viscoelastic fluid depends on various factors including elasticity, inertia, shear thinning/thickening, initial distance and configuration. Despite these complex features, both experiments and simulations confirm that particle aggregation is enhanced by normal stresses induced by elasticity (cf. Zenit & Feng 2018, for detailed review). Since particle clustering and wake dynamics, even at low concentrations, significantly affect the turbulence (Uhlmann & Doychev 2014; Capecelatro, Desjardins & Fox 2018), we dedicate this section to the study of particle microstructures in our simulations.

The radial distribution function (RDF) is a common first-order measure of particle clustering in suspensions (Shaw 2003). It is defined as the average number of particles $\langle dN \rangle$ located at a spherical shell of radius r and thickness dr , and which is centred at the reference particle position \mathbf{P}_{ref} . In a homogeneous system of point particles, the RDF is commonly normalized by the same quantity for a random distribution of points in the space (Reade & Collins 2000). In our system, however, due to the presence of a strong heterogeneity in the y direction, as well as the non-overlapping condition for finite-sized particles, an unbiased analysis calls for a tailored normalization. We define $g(r)$ in the limit $dr \rightarrow 0$ by,

$$g(r) = \langle dN(r) \rangle / \langle dN(r)^R \rangle, \quad (4.3)$$

$$dN(r) = \sum_{m=1}^{N_p} \delta(r - |r_m|), \quad (4.4)$$

$$\mathbf{r}_m = \mathbf{P}_m - \mathbf{P}_{ref}, \quad (4.5)$$

where \mathbf{P} and $\delta(r)$ are the position vector and Dirac delta function. The averaging operation is performed over all particles at a given y location at different instances of time. The superscript 'R' indicates that the quantity is measured for a random distribution of points seeded in the same domain as our DNS dataset, with the following two additional constraints: (i) the minimum distance between two points is always larger than a particle diameter (non-overlapping condition); (ii) the distribution of the points in the y direction matches that of the DNS dataset within 0.5 % error. The latter condition ensures that $g(r)$ is not biased by the heterogeneity in the y direction and that any deviation of $g(r)$ from unity is a signature of a local aggregation/segregation of particles.

Figure 16 shows the RDF in the near-wall and channel centre regions. The value of $g(r)$ is expectedly high at a separation approximately equal to one particle diameter in the Newtonian and viscoelastic cases, because the collision force in that region stabilizes particle pairs. The peak is, however, more than twofold higher in the viscoelastic cases, which signals an increase in the formation of particle pairs. At the channel centre, the propensity of elasticity is slightly reduced. The RDF rapidly tends to the unity at both wall-normal heights, be that for the Newtonian or viscoelastic flows, which indicates absence of any long-range particle structure.

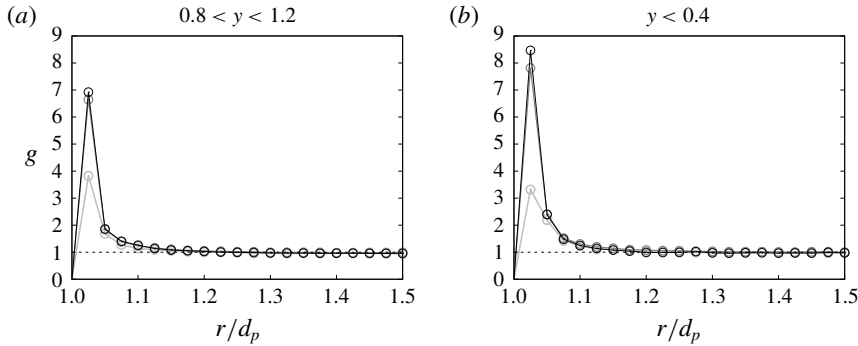


FIGURE 16. Radial distribution function (4.3) with reference position in the region (a) $0.8 < y < 1.2$ and (b) $y < 0.4$. Line types as listed in table 1: (—○) WOP5; (—□) W15P5; (—△) W25P5.

In laminar viscoelastic flows, particle pairs initially aligned in a cross-stream configuration experience a strong attraction due to the normal stresses (Goyal & Derksen 2012; Zenit & Feng 2018). If the initial configuration is alignment in the streamwise direction, repulsion or attraction of the particle pairs is determined by their initial distance: a distance larger than a critical value, which itself is inversely proportional to viscoelasticity, results in repulsion due to the negative wake of the leading particle. Therefore, provided elasticity is sufficiently high, repulsion takes place regardless of initial separation (D’Avino, Hulsen & Maffettone 2013). In suspensions, the co-existence of these effects may give rise to more complex structures such as particle chains (Zenit & Feng 2018). The microstructure of particles, and specifically preferential directionality in particle-pair alignment, is examined in our simulations.

We define the particle-pair distribution function, $q(r, \psi, \theta)$, which depends on the pair separation r , the polar angle ψ relative to the positive z axis and the azimuthal angle θ measured counterclockwise from the positive x axis,

$$q(r, \psi, \theta) = \langle dN(r, \psi, \theta) \rangle / \langle dN(r, \psi, \theta)^R \rangle, \tag{4.6}$$

$$dN(r, \theta) = \sum_{m=1}^{N_p} \delta(r - |\mathbf{r}_m|) \delta(\theta - \theta_m), \delta(\psi - \psi_m), \tag{4.7}$$

$$\mathbf{r}_m = \mathbf{P}_{ref} - \mathbf{P}_m, \tag{4.8}$$

$$\psi_m = \cos^{-1} \left(\frac{\mathbf{r}_m \cdot \mathbf{e}_z}{|\mathbf{r}_m|} \right); \quad \phi_m = \arctan \left(\frac{\mathbf{r}_m \cdot \mathbf{e}_y}{\mathbf{r}_m \cdot \mathbf{e}_x} \right), \tag{4.9a,b}$$

where $\mathbf{e}_{\{x,y,z\}}$ are the unit vectors along the Cartesian coordinates. Similar to the RDF, averaging is performed over the ensemble of reference particles located at a given y location at different instances of time, and superscript ‘ R ’ indicates a random distribution conditioned in a similar manner as in the computation of the RDF. Figure 17(a–c) compares q for the different cases at the channel centre. Due to symmetry at this location, the azimuthal angle is only plotted in the range $0 < \theta < \pi$. The narrow stripe with high values of q immediately surrounding the particle, near $r = 1$, highlights the strong effect of particle collisions in stabilizing particle pairs.

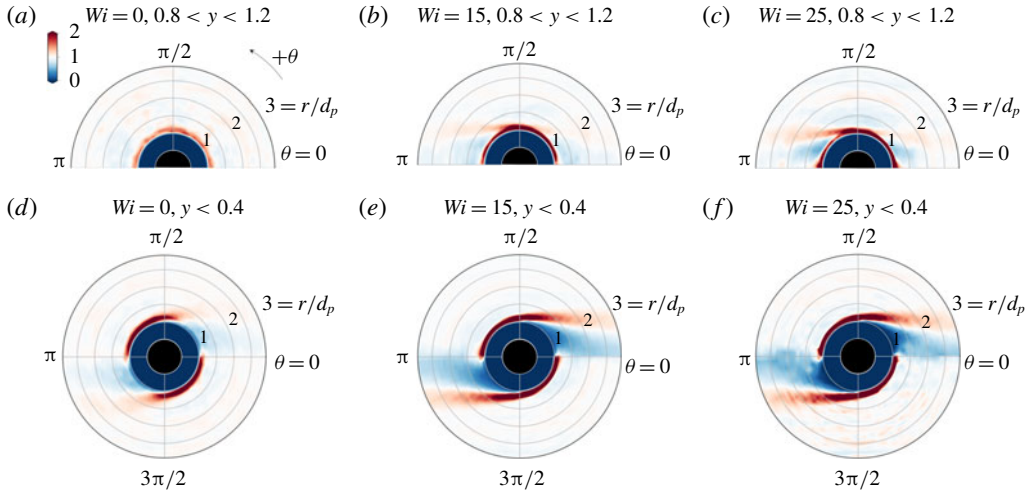


FIGURE 17. (Colour online) Particle-pair distribution function $q(r, \psi, \theta)$, averaged in the range $-\pi/8 < \psi - \pi/2 < \pi/8$. Reference particle is located in the region (a,b,c) $0.8 < y < 1.2$ and (d,e,f) $y < 0.4$.

This effect is intensified in the viscoelastic cases, in line with the RDF results. It should be noted that, due to the absence of shear and slip velocity, we do not observe any significant preferential alignment of particle pairs near the channel centre in the Newtonian or viscoelastic cases.

The particle-pair distribution function near the wall is reported in figure 17(d–f). In all three panels, two narrow stripes with high values of q are observed immediately around the particle in the two quadrants $\pi/2 < \theta < \pi$ and $3\pi/2 < \theta < 2\pi$. They arise, respectively, due to the deficit and excess particle phase velocity relative to the local fluid in the presence of mean shear – an effect that has been reported for suspensions with a Newtonian carrier fluid (Morris 2009). A relative depletion of particles occurs in the straining quadrants $0 < \theta < \pi/2$ and $\pi < \theta < 3\pi/2$, evidenced by a region of lower probability of finding a particle pair. Viscoelasticity results in two unique features: (i) the particle-free regions are markedly extended in the streamwise direction and (ii) q increases at the outer edges of these two regions which indicates that an inclined alignment with respect to the streamwise coordinate is promoted. In order to explain these effects, we evaluated the particle-conditioned mean streamwise velocity $\langle u_f \rangle_{pc}$ relative to $\langle u_f \rangle$. A positive and a negative isosurface of $\langle u_f \rangle_{pc} - \langle u_f \rangle$ are shown in figure 18 for case W15P5. The isosurfaces extend downstream and upstream of the reference particle, respectively, and their effect is to expel leading and trailing particles, consistent with the streamwise extended regions of low q in figure 17(b).

4.3. Flow visualization

In order to obtain a precise interpretation of the flow in the vicinity of the particle, we evaluate the average flow field conditioned on the particle position and also the particle slip velocity. Figure 19 shows results for particles whose centre is at $y = 0.1$ and whose slip velocity is $u_{slip} = 0.05$, from the Newtonian and W15P5 cases. The conditionally averaged in-plane velocity vectors and contours of their streamwise

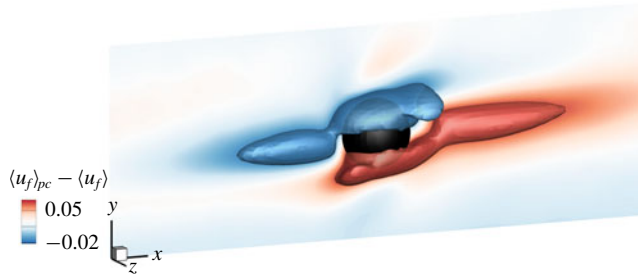


FIGURE 18. (Colour online) Particle-conditioned mean streamwise fluid velocity $\langle u_f \rangle_{pc}$ relative to $\langle u_f \rangle$, for case W15P5. The conditional average is performed for particles located at $y = 0.2$.

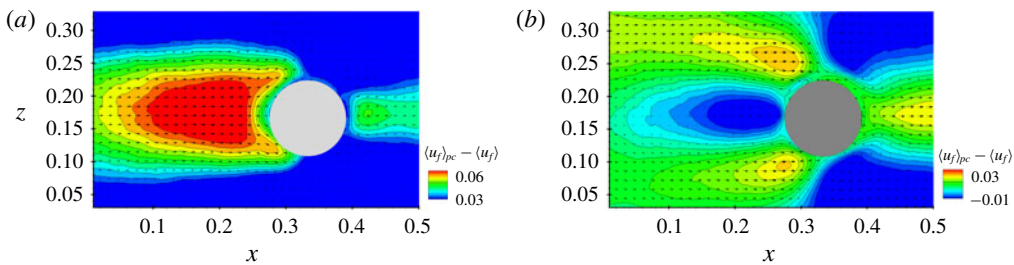


FIGURE 19. (Colour online) Particle-conditioned mean flow field relative to the unconditional fluid velocity, $\langle u_f \rangle_{pc} - \langle u_f \rangle$. The conditional average is performed for particles located at $y = 0.1$ and which experience $u_{slip} = 0.05$. Contours show the streamwise component, and the vectors correspond to the in-plane velocities. (a) WOP5; (b) W15P5.

components are reported after subtracting the mean fluid velocity $\langle u_f \rangle$. The flow fields are dramatically different in the wake regions: a classic backwash behind the particle is observed in case WOP5; in contrast, a negative zone in the trail of the particle in case W15P5 signals the presence of a reverse wake which is enfolded by a conical entraining zone of accelerated fluid. It should be noted that the negative zone in the contours of $\langle u_f \rangle_{pc} - \langle u_f \rangle$ is a signature of decelerated streamwise velocity only, while u_f is almost never negative in an absolute sense. Similar wake patterns have been previously observed in experiments (Kemiha *et al.* 2006) and simulations (Frank & Li 2006; Goyal & Derksen 2012) of an isolated rising bubble or falling solid sphere in extensional flows. Compared to those studies, however, the negative wake and the positive cone are spatially truncated due to the presence of neighbouring particles in our cases. According to the 2-D axisymmetric numerical simulations by Frank & Li (2006), where the Reynolds number based on the particle diameter is more than unity, the opening angle of the conical zone is independent of the Reynolds number, while it is weakly and inversely correlated with the Weissenberg number. The wake characteristics in figure 19(b) explain the peculiar particle microstructure observed in the viscoelastic cases (cf. figure 17): while the negative wake repels the trailing particles, the entrainment zone stabilizes particle pairs with an inclined alignment with respect to the streamwise direction.

Figure 20 shows instantaneous plan views of the streamwise component of the polymer stress tensor at $y = 0.1$, from cases W15 and W15P5; two isolevels of

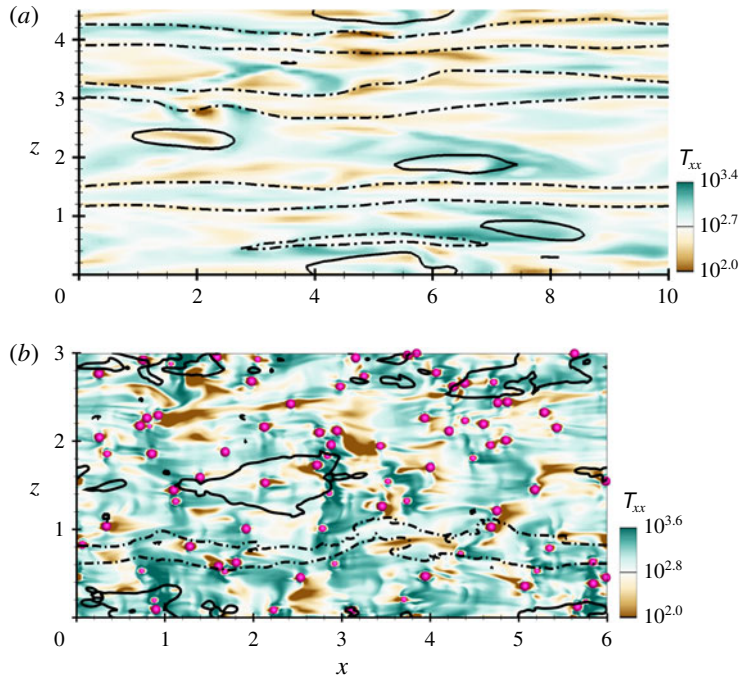


FIGURE 20. (Colour online) Instantaneous contours of the streamwise component of the polymer stress tensor T_{xx} at $y = 0.1$. (a): W15; (b) W15P5. Lines are isocontours of (solid lines —) positive and (dash-dotted lines -.-) negative streamwise velocity perturbations, $u_f - \langle u_f \rangle$. Pink circles mark the positions of particles that are cut by the xz plane.

streamwise velocity perturbation are also marked. In case W15, the high- and low-stress regions have similar shapes and length scale as the isolines of velocity perturbations; the co-location of the stress and velocity perturbations is qualitatively indicative of the connection between turbulent structures and polymer stretch. It should be noted that, for the sake of clarity of the visualization, the isolines are plotted for one positive and one negative value of the velocity perturbation only, and thus do not represent all the turbulent structures. In contrast, there is no conspicuous similarity between region of high/low polymer stress regions and the isolines of velocity perturbations in case W15P5. As a matter of fact, the polymer stress is mostly concentrated in the vicinity of the particles, which highlights the change in the dominant stretch mechanism in particle-laden conditions (cf. § 4.1).

Instantaneous visualizations of streamwise flow structures and particle positions are provided in figure 21. The figure contrasts realizations from the single-phase and particle-laden simulations, for the Newtonian fluids and at $Wi = 15$; for the latter case, the active and hibernating states are shown. These instantaneous fields encapsulate some important conclusions drawn in the previous sections: (i) particles weaken the streamwise streaks in Newtonian and viscoelastic flows; (ii) the modulation of turbulent structures is relatively minimal in the Newtonian case and pronounced in the viscoelastic flows; (iii) particles migrate towards the channel centre during hibernating states, and back towards the wall during active intervals. Additionally, the wake-induced fluid fluctuations are discernible in the near-wall region of the viscoelastic condition, particularly during the active turbulence period.

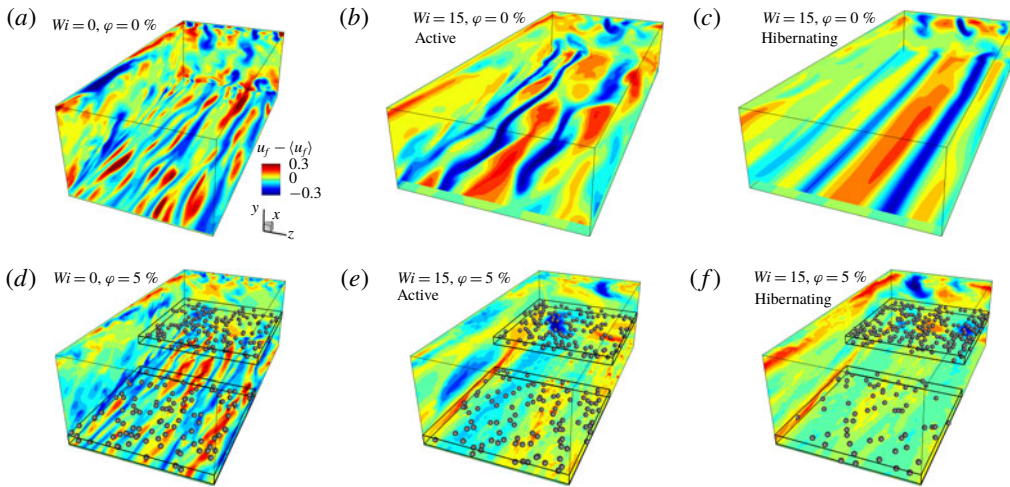


FIGURE 21. (Colour online) Instantaneous contours of $u_f - \langle u_f \rangle$ in the (a,d) Newtonian flows, and in the lower Weissenberg viscoelastic cases during (b,e) active and (c,f) hibernating states. (a–c) Single-phase simulations; (d–f) two-phase simulations. Particle positions are visualized in two sub-regions of the domain, near the wall and at channel centre. The horizontal planes are visualized at $y^+ \approx 8$ in all cases.

5. Conclusion

The effects of neutrally buoyant spherical particles on viscoelastic turbulent channel flow were examined using direct numerical simulations. The particles are larger than the dissipation length scale, and the flow is resolved at the scale of the particles with an immersed boundary method. The particle-laden cases with bulk solid volume fraction $\varphi = 5\%$ were compared to their single-phase counterparts, while the Reynolds number was fixed at $Re = 2800$ for all cases. Additionally, two different Weissenberg numbers were considered in comparison to the Newtonian configurations.

The particles enhance the overall drag in the Newtonian and viscoelastic flows, relative to the single-phase configurations. The drag increase is, however, more appreciable in the viscoelastic cases; a similar observation was made based on the recent experimental measurements by Zade *et al.* (2019). The present simulations demonstrate that a significant contribution is due to the particles increasing the polymer stress by stretching the polymer chains in their vicinity.

Despite the overall increase in drag, the turbulence activity is appreciably suppressed in the presence of particles. In Newtonian flows, the reduction of the streamwise fluctuations was previously explained by the propensity of the particles to weaken the streamwise streaks (Shao *et al.* 2012).

In the viscoelastic cases, the particle attenuation of the turbulent fluctuations is dramatically higher. We examined this effect in further detail by evaluating conditional averages of the flow statistics and particle concentration in the hibernating and active turbulence states: the particles systematically migrated towards the channel centre during the former and back towards the wall by relatively strong turbulence motions during the latter. Overall, the particles promote the hibernating state of the turbulence, thus reducing the average turbulent stresses.

The mean streamwise particle velocity follows the local fluid velocity in most of the channel, except in the near-wall region. In the viscoelastic cases, the particle

mean speed is smaller than that of the fluid above the viscous sublayer. Following Kidanemariam *et al.* (2013), we investigated this effect by estimating the velocity experienced by the particles on a local trimmed spherical shell. We found that particles tend to preferentially reside in the low-speed regions of the flow; this effect is also known to take place in Newtonian wall-bounded turbulence for particles of the order of the Kolmogorov scale (Pan & Banerjee 1997) and up to $d_p^+ \approx 5\text{--}10$ (Kidanemariam *et al.* 2013; Wang *et al.* 2018). In our simulations, it was observed for larger particles in the viscoelastic cases $d_p^+ \approx 15$, potentially due to the swelling of the turbulent structures. A comprehensive study of different particle sizes is, nonetheless, required to further verify this hypothesis. Furthermore, while this phenomenon is accompanied by the formation of long streaks of particles in the case of Newtonian flows (Pan & Banerjee 1997), we have not observed such structures in our particle-laden viscoelastic cases. In contrast, by studying the particle-pair distribution function, we demonstrated that the probability of finding a particle pair aligned in the streamwise direction is significantly lower in the viscoelastic cases. This finding was explained by examining the conditionally averaged velocity field in the vicinity of the particle, which acts to expel particles leading or trailing the reference one.

The present study highlights the richness of phenomenology in particle-laden viscoelastic turbulence and motivates new research directions. Studies of controlled configurations, for example with an isolated particle similar to the Newtonian efforts by Naso & Prosperetti (2010), are needed. And since particle migration in Newtonian fluids is known to be dependent strongly on their response time and gravitational effects (Kidanemariam *et al.* 2013; Fornari *et al.* 2016), the influence of these parameters must be evaluated in the presence of fluid elasticity.

Acknowledgements

This work was supported in part by the National Science Foundation (grants 1511937 and 1804004). Computational resources were provided by the Maryland Advanced Research Computing Center (MARCC). The authors thank Dr S. J. Lee and Dr I. Hameduddin for their contributions to the legacy code that was the starting point of the numerical algorithm used in this work.

Appendix A. Conditionally averaged momentum balance

The present derivation follows the general approach by Zhang & Prosperetti (2010), with an eye to other similar derivations for Newtonian flows (Pope 2000; Picano *et al.* 2015). For a control volume \mathcal{V}^* Newton's second law has the form,

$$\int_{\mathcal{V}^*} [(1 - \chi)\rho_f^* \mathbf{a}_f^* + \chi\rho_p^* \mathbf{a}_p^*] d\mathcal{V}^* = \oint_{\partial\mathcal{V}^*} [(1 - \chi)\boldsymbol{\sigma}_f^* + \chi\boldsymbol{\sigma}_p^*] \cdot \mathbf{n} dA^* + \int_{\mathcal{V}^*} [(1 - \chi)\rho_f^* + \chi\rho_p^*] \mathbf{g}^* d\mathcal{V}^*, \quad (\text{A } 1)$$

where $\rho_{\{f,p\}}^*$, $\mathbf{a}_{\{f,p\}}^*$ and $\boldsymbol{\tau}_{\{f,p\}}^*$ are the density, acceleration and stress tensor of the fluid 'f' and particle 'p'. The unit vector \mathbf{n} is outwardly normal to the control surfaces $\partial\mathcal{V}^*$, and \mathbf{g}^* is a generic body force per unit mass equal in both phases. For matching fluid and particle densities $\rho_f^* = \rho_p^*$, and in the absence of any body force, the ensemble average of equation (A 1) is,

$$\rho_f^* \int_{\mathcal{V}^*} [(1 - \phi)\langle \mathbf{a}_f^* \rangle + \phi\langle \mathbf{a}_p^* \rangle] d\mathcal{V}^* = \oint_{\partial\mathcal{V}^*} [(1 - \phi)\langle \boldsymbol{\sigma}_f^* \rangle + \phi\langle \boldsymbol{\sigma}_p^* \rangle] \cdot \mathbf{n} dA^*. \quad (\text{A } 2)$$

Using the divergence theorem, the surface integral on the right-hand side of (A 2) is transformed into a volume integral,

$$\rho_f^* \int_{\mathcal{V}^*} [(1 - \phi)\langle \mathbf{a}_f^* \rangle + \phi\langle \mathbf{a}_p^* \rangle] d\mathcal{V}^* = \int_{\mathcal{V}^*} \nabla \cdot [(1 - \phi)\langle \boldsymbol{\sigma}_f^* \rangle + \phi\langle \boldsymbol{\sigma}_p^* \rangle] d\mathcal{V}^*. \quad (\text{A } 3)$$

And since the control volume is arbitrary, (A 3) can be rewritten in differential form,

$$\rho_f^* [(1 - \phi)\langle \mathbf{a}_f^* \rangle + \phi\langle \mathbf{a}_p^* \rangle] = \nabla \cdot [(1 - \phi)\langle \boldsymbol{\sigma}_f^* \rangle + \phi\langle \boldsymbol{\sigma}_p^* \rangle]. \quad (\text{A } 4)$$

Assuming continuity for both phases, expanding the material derivatives and expressing the fluid stress tensor in terms of the solvent and polymer contributions, equation (A 4) becomes,

$$\begin{aligned} (1 - \phi) \frac{\partial \langle \mathbf{u}_f^* \rangle}{\partial t^*} + (1 - \phi) \langle \mathbf{u}_f^* \cdot \nabla \mathbf{u}_f^* \rangle + \phi \frac{\partial \langle \mathbf{u}_p^* \rangle}{\partial t^*} + \phi \langle \mathbf{u}_p^* \cdot \nabla \mathbf{u}_p^* \rangle \\ = -\nabla [\beta(1 - \phi)\langle p^* / \rho_f^* \rangle] + \nabla \cdot [2\beta(1 - \phi)v^* \langle \mathbf{E}^* / \rho_f^* \rangle] \\ + \nabla \cdot [(1 - \beta)(1 - \phi)\langle \mathbf{T}^* / \rho_f^* \rangle] + \nabla \cdot (\phi\langle \boldsymbol{\sigma}_p^* / \rho_f^* \rangle), \end{aligned} \quad (\text{A } 5)$$

or in dimensionless form,

$$\begin{aligned} (1 - \phi) \frac{\partial \langle \mathbf{u}_f \rangle}{\partial t} + (1 - \phi) \langle \mathbf{u}_f \cdot \nabla \mathbf{u}_f \rangle + \phi \frac{\partial \langle \mathbf{u}_p \rangle}{\partial t} + \phi \langle \mathbf{u}_p \cdot \nabla \mathbf{u}_p \rangle \\ = -\nabla [\beta(1 - \phi)\langle p \rangle] + \nabla \cdot \left[\frac{2\beta}{Re}(1 - \phi)\langle \mathbf{E} \rangle \right] \\ + \nabla \cdot \left[\frac{(1 - \beta)}{Re}(1 - \phi)\langle \mathbf{T} \rangle \right] + \nabla \cdot (\phi\langle \boldsymbol{\sigma}_p \rangle). \end{aligned} \quad (\text{A } 6)$$

For statistically stationary flows, the time derivatives of the mean fluid and particle velocities vanish. In addition, by taking into account that $\mathbf{u}_{\{f,p\}} = \langle \mathbf{u}_{\{f,p\}} \rangle + \mathbf{u}'_{\{f,p\}}$, equation (A 6) becomes,

$$\begin{aligned} (1 - \phi) \langle \mathbf{u}_f \rangle \cdot \nabla \langle \mathbf{u}_f \rangle + (1 - \phi) \nabla \cdot \langle \mathbf{u}'_f \mathbf{u}'_f \rangle + \phi \langle \mathbf{u}_p \rangle \cdot \nabla \langle \mathbf{u}_p \rangle + \phi \nabla \cdot \langle \mathbf{u}'_p \mathbf{u}'_p \rangle \\ = -\nabla [\beta(1 - \phi)\langle p \rangle] + \nabla \cdot \left[\frac{2\beta}{Re}(1 - \phi)\langle \mathbf{E} \rangle \right] \\ + \nabla \cdot \left[\frac{(1 - \beta)}{Re}(1 - \phi)\langle \mathbf{T} \rangle \right] + \nabla \cdot (\phi\langle \boldsymbol{\sigma}_p \rangle). \end{aligned} \quad (\text{A } 7)$$

Exploiting homogeneity in the streamwise and spanwise directions, the mean-momentum equation in the wall-normal direction reduces to,

$$\begin{aligned} \frac{d[(1 - \phi)\langle v'_f v'_f \rangle]}{dy} + \frac{d[\phi\langle v'_p v'_p \rangle]}{dy} + \frac{d[\beta(1 - \phi)\langle p \rangle]}{dy} \\ - \frac{d\left[\frac{1 - \beta}{Re}(1 - \phi)\langle T_{yy} \rangle\right]}{dy} - \frac{d[\phi\langle \sigma_{p,yy} \rangle]}{dy} = 0. \end{aligned} \quad (\text{A } 8)$$

Equation (A 8) is integrated in the y-direction between two impermeable walls to yield,

$$\begin{aligned}
 & (1 - \phi)\langle v'_f v'_f \rangle + \phi\langle v'_p v'_p \rangle + \beta(1 - \phi)\langle p \rangle - \frac{1 - \beta}{Re}(1 - \phi)\langle T_{yy} \rangle - \phi\langle \sigma_{p,yy} \rangle \\
 & = \beta(1 - \phi)\langle p^{wall} \rangle - \frac{1 - \beta}{Re}(1 - \phi)\langle T_{yy}^{wall} \rangle - \phi\langle \sigma_{p,yy}^{wall} \rangle.
 \end{aligned} \tag{A 9}$$

Taking the derivative with respect to x and exploiting homogeneity in the streamwise direction to eliminate the Reynolds stresses, we obtain

$$\begin{aligned}
 & \frac{d}{dx} \left[\beta(1 - \phi)\langle p \rangle - \frac{1 - \beta}{Re}(1 - \phi)\langle T_{yy} \rangle - \phi\langle \sigma_{p,yy} \rangle \right] \\
 & = \frac{d}{dx} \left[\beta(1 - \phi)\langle p^{wall} \rangle - \frac{1 - \beta}{Re}(1 - \phi)\langle T_{yy}^{wall} \rangle - \phi\langle \sigma_{p,yy}^{wall} \rangle \right].
 \end{aligned} \tag{A 10}$$

Similarly, the mean-momentum equation (A 7) in the streamwise direction is,

$$\begin{aligned}
 & \frac{d}{dy} \left[-(1 - \phi)\langle u'_f v'_f \rangle - \phi\langle u'_p v'_p \rangle + \frac{\beta}{Re}(1 - \phi)\frac{d\langle u_f \rangle}{dy} + \right. \\
 & \quad \left. + \frac{(1 - \beta)}{Re}(1 - \phi)\langle T_{xy} \rangle + \phi\langle \sigma_{p,xy} \rangle \right] \\
 & = \frac{d}{dx} \left[\beta(1 - \phi)\langle p \rangle - \frac{(1 - \beta)}{Re}(1 - \phi)\langle T_{xx} \rangle - \phi\langle \sigma_{p,xx} \rangle \right].
 \end{aligned} \tag{A 11}$$

Using (A 10), the right-hand side of equation (A 11) can be rewritten as,

$$\begin{aligned}
 & \frac{d}{dy} \left[-(1 - \phi)\langle u'_f v'_f \rangle - \phi\langle u'_p v'_p \rangle + \frac{\beta}{Re}(1 - \phi)\frac{d\langle u_f \rangle}{dy} + \right. \\
 & \quad \left. + \frac{(1 - \beta)}{Re}(1 - \phi)\langle T_{xy} \rangle + \phi\langle \sigma_{p,xy} \rangle \right] \\
 & = \frac{d}{dx} \left[\beta(1 - \phi)\langle p^{wall} \rangle - \frac{(1 - \beta)}{Re}(1 - \phi)\langle T_{xx}^{wall} \rangle - \phi\langle \sigma_{p,xx}^{wall} \rangle \right. \\
 & \quad \left. - \frac{(1 - \beta)}{Re}(1 - \phi)(\langle T_{yy} \rangle - \langle T_{xx} \rangle) - \phi(\langle \sigma_{p,yy} \rangle - \langle \sigma_{p,xx} \rangle) \right].
 \end{aligned} \tag{A 12}$$

Due to the homogeneity in the streamwise direction, $d(\langle T_{yy} \rangle - \langle T_{xx} \rangle)/dx$ and $d(\langle \sigma_{p,yy} \rangle - \langle \sigma_{p,xx} \rangle)/dx$ vanish. The remaining terms on the right-hand side of (A 12) are all associated with the wall and independent of y , while the left-hand side terms are exclusively a function of y due to homogeneity in the x and z directions. Hence, it is evident that both sides of (A 12) are constant. In compact form,

$$\frac{d\tau_{tot}}{dy} = \text{const.}, \tag{A 13}$$

where τ_{tot} is total mean shear stress of the mixture and is a linear function of y only. Since τ_{tot} is symmetric with respect to the channel centre at $y = 1$, integrating (A 13)

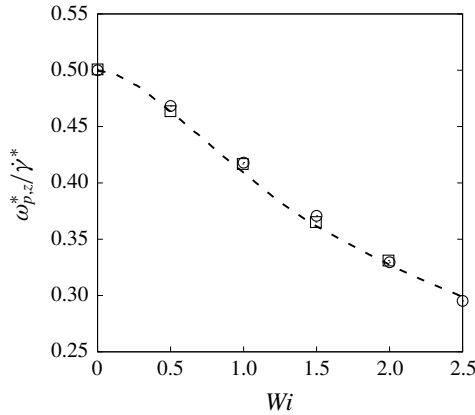


FIGURE 22. Rotation rate of a sphere in simple shear as a function of the Weissenberg number: (---) experimental measurements by Snijkers *et al.* (2011); (\square) numerical simulations by Goyal & Derksen (2012); (\circ) present results.

in y yields,

$$\begin{aligned} \tau_{tot}(y) = & -[(1 - \phi)\langle u'_f v'_f \rangle + \phi\langle u'_p v'_p \rangle] + \frac{\beta}{Re}(1 - \phi) \frac{d\langle u_f \rangle}{dy} \\ & + \frac{(1 - \beta)}{Re}(1 - \phi)\langle T_{xy} \rangle + \phi\langle \sigma_{p,xy} \rangle = \langle \tau_{wall} \rangle(1 - y). \end{aligned} \quad (A 14)$$

Appendix B. Reference simulations and validation of the algorithm

B.1. Freely rotating sphere in simple shear

Data from experiments (Snijkers *et al.* 2011) and numerical simulations (D’Avino *et al.* 2008; Goyal & Derksen 2012) of a sphere in simple shear are used for validation of the particle-laden viscoelastic flow solver. Computations are performed in a rectangular domain with size $(4 \times 4 \times 2)d_p^*$, and a particle with diameter d_p^* is initially located at the centre. The flow has a constant shear rate $\dot{\gamma}^*$, and is induced by two parallel plates located at $y^* = \{0, 4d_p^*\}$, moving opposite to one another in the x and z directions. In Newtonian fluids at low Reynolds numbers, the shear flow induces particle rotation at an angular velocity $\omega_{p,z}^* = \dot{\gamma}^*/2$. The prescribed Reynolds number is $\dot{\gamma}^* d_p^{*2}/4\nu^* = 0.025$, and the viscosity ratio $\beta = 0.5$. Similar to our main particle-laden simulations, sixteen grid points span the particle diameter.

In viscoelastic flows, Snijkers *et al.* (2011) showed that the rotation rate of the sphere monotonically decreases with increasing Weissenberg number, $Wi = \dot{\gamma}^* \lambda^*$. As shown in figure 22, agreement between the experimental results and our numerical predictions in particle angular velocity is satisfactory. Results from the numerical simulations by Goyal & Derksen (2012) are also presented for comparison.

B.2. Lateral migration of isolated particle in Poiseuille flow

Migration of a neutrally buoyant spherical particle is simulated in laminar Poiseuille flow. We first validate our numerical algorithm by predicting the particle equilibrium position in a Newtonian case. Following Loisel *et al.* (2013), we set the particle

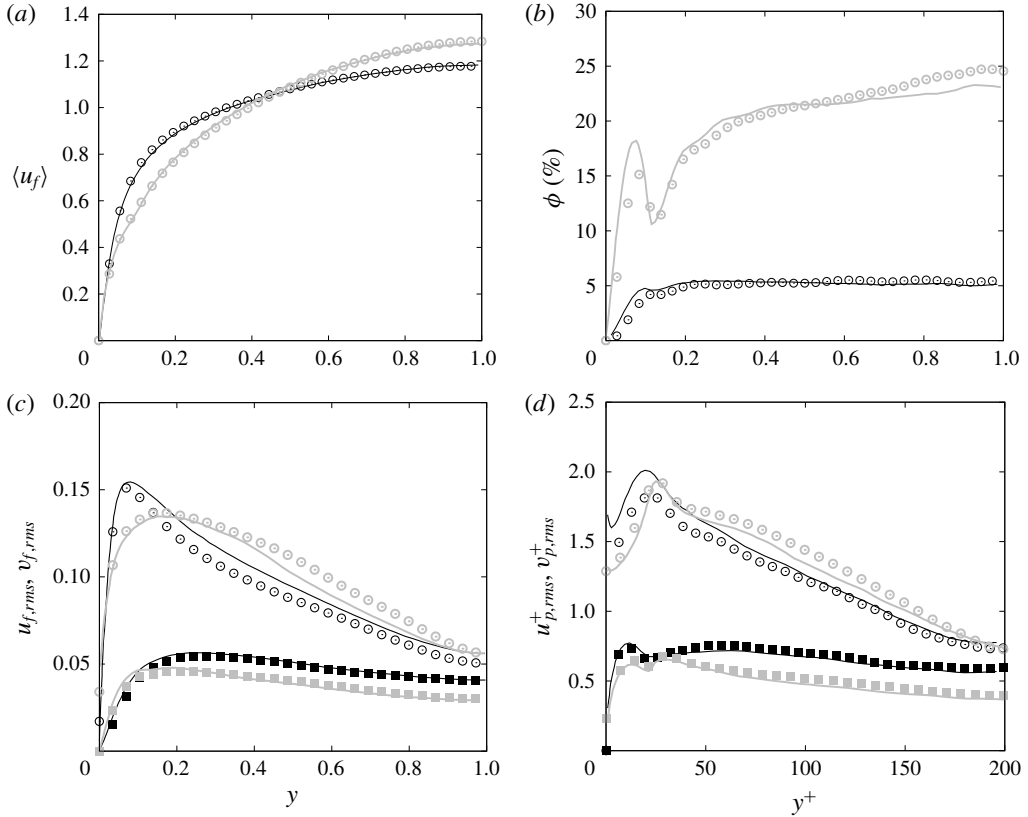


FIGURE 23. Comparison of DNS data (solid lines) by Picano *et al.* (2015) and (symbols) from the present study. Black and grey colours correspond to bulk solid volume fractions $\phi = \{5, 20\}$ %, respectively. Profiles of (a) mean fluid velocity, (b) solid volume fraction, (c,d) streamwise and wall-normal velocity fluctuations in the fluid and particles, the latter plotted in wall units. (c,d) (circles, \circ) streamwise fluctuations; (squares, \blacksquare) wall-normal fluctuations.

d_p^*/h^*	Re	β, L_{max}	El	y_{eq}^*/h^*	y_{eq}^*/h^* (Asmolov 1999)	γ_{eq}^*/h^* (Loisel <i>et al.</i> 2013)
		Newtonian	0	0.1991	0.2061	0.1916
1/8	100	FENE-P	15/2800	0.2132	—	—
		$\beta = 0.97$	25/2800	0.2211	—	—
		$L_{max} = 70$				

TABLE 2. Parameters of the simulations of isolated particle in Poiseuille flow and the final equilibrium positions.

diameter to $d_p^*/h^* = 1/8$ and the Reynolds number to $U_b^*h^*/\nu^* = 100$. We adopt the same grid resolution as in the main computations, $\Delta x^* = d_p^*/16$. The sizes of the simulation domain are $(16 \times 16 \times 4)d_p^*$ in the streamwise, wall-normal and spanwise directions. The boundary conditions in the horizontal directions are periodic and no slip is applied at the bottom and top walls. Table 2 summarizes the physical parameters and the final equilibrium positions in comparison to results reported in the literature. After the initial transient, the particle reaches an equilibrium position

$y_{eq}^*/h^* = 0.1991$, which is within the two values reported by Asmolov (1999) and Loisel *et al.* (2013).

In order to demonstrate the effect of elasticity on particle migration, we perform two additional simulations using FENE-P fluids at the same Reynolds number. The elasticity number $El \equiv Wi/Re = \lambda^*v^*/h^{*2}$, viscosity ratio β and maximum extensibility L_{max} are selected such that they match those of cases W15P5 and W25P5. The computed equilibrium positions of the particles are further away from the wall (see table 2). This effect is due to the elastic forces which decrease as the particle approaches the channel centre.

B.3. Newtonian particle-laden turbulent channel flow

Two DNS datasets by Picano *et al.* (2015) are compared to results using our numerical algorithm. The configuration and parameters of one dataset are equivalent to those of case W0P5 in the present study (§ 2.3), while the second dataset has a higher bulk solid volume fraction $\varphi = 20\%$. For the latter case, we adopt the soft-sphere potential with a sub-grid-scale lubrication correction in order to model particle–particle and particle–wall collisions, similar to Picano *et al.* (2015). We also adopt the same grid resolution, $\Delta x = d_p/16$.

A number of wall-normal profiles are shown in figure 23. Evidently, our numerical simulations are in good qualitative and quantitative agreement with the reference results, especially for the higher volume fraction where conditions are more closely matched. Minor inconsistencies, specifically in the low concentration case and in particle statistics which require long simulation times for convergence, are sufficiently small and do not result in any bias in related conclusions.

REFERENCES

- AGARWAL, A., BRANDT, L. & ZAKI, T. A. 2014 Linear and nonlinear evolution of a localized disturbance in polymeric channel flow. *J. Fluid Mech.* **760**, 278–303.
- ARDEKANI, M. N. & BRANDT, L. 2019 Turbulence modulation in channel flow of finite-size spheroidal particles. *J. Fluid Mech.* **859**, 887–901.
- ASMOLOV, E. S. 1999 The inertial lift on a spherical particle in a plane Poiseuille flow at large channel Reynolds number. *J. Fluid Mech.* **381**, 63–87.
- BALACHANDAR, S. & EATON, J. K. 2010 Turbulent dispersed multiphase flow. *Annu. Rev. Fluid Mech.* **42** (1), 111–133.
- BARBATI, A. C., DESROCHES, J., ROBISSON, A. & MCKINLEY, G. H. 2016 Complex fluids and hydraulic fracturing. *Annu. Rev. Chem. Biomol. Engng* **7**, 415–453.
- BIANCOFIORE, L., BRANDT, L. & ZAKI, T. A. 2017 Streak instability in viscoelastic Couette flow. *Phys. Rev. Fluids* **2**, 043304.
- BREUGEM, W. P. 2012 A second-order accurate immersed boundary method for fully resolved simulations of particle-laden flows. *J. Comput. Phys.* **231** (13), 4469–4498.
- CAPECELATRO, J., DESJARDINS, O. & FOX, R. O. 2018 On the transition between turbulence regimes in particle-laden channel flows. *J. Fluid Mech.* **845**, 499–519.
- CAPORALONI, M., TAMPPIERI, F., TROMBETTI, F. & VITTORI, O. 1975 Transfer of particles in nonisotropic air turbulence. *J. Atmos. Sci.* **32**, 565–568.
- CHOEIRI, G. H., LOPEZ, J. M. & HOF, B. 2018 Exceeding the asymptotic limit of polymer drag reduction. *Phys. Rev. Lett.* **120** (12), 124501.
- CISSE, M., HOMANN, H. & BEC, J. 2013 Slipping motion of large neutrally buoyant particles in turbulence. *J. Fluid Mech.* **735**, R1.
- COSTA, P., PICANO, F., BRANDT, L. & BREUGEM, W. P. 2016 Universal scaling laws for dense particle suspensions in turbulent wall-bounded flows. *Phys. Rev. Lett.* **117** (13), 1–5.

- COSTA, P., PICANO, F., BRANDT, L. & BREUGEM, W. P. 2018 Effects of the finite particle size in turbulent wall-bounded flows of dense suspensions. *J. Fluid Mech.* **843**, 450–478.
- DALLAS, V., VASSILICOS, J. C. & HEWITT, G. F. 2010 Strong polymer-turbulence interactions in viscoelastic turbulent channel flow. *Phys. Rev. E* **82** (6), 1–19.
- D'AVINO, G., GRECO, F. & MAFFETTONE, P. L. 2017 Particle migration due to viscoelasticity of the suspending liquid and its relevance in microfluidic devices. *Annu. Rev. Fluid Mech.* **49** (1), 341–360.
- D'AVINO, G., HULSEN, M. A. & MAFFETTONE, P. L. 2013 Dynamics of pairs and triplets of particles in a viscoelastic fluid flowing in a cylindrical channel. *Comput. Fluids* **86**, 45–55.
- D'AVINO, G., HULSEN, M. A., SNIJKERS, F., VERMANT, J., GRECO, F. & MAFFETTONE, P. L. 2008 Rotation of a sphere in a viscoelastic liquid subjected to shear flow. Part I. Simulation results. *J. Rheol.* **52** (6), 1331–1346.
- DE LILLO, F., BOFFETTA, G. & MUSACCHIO, S. 2012 Control of particle clustering in turbulence by polymer additives. *Phys. Rev. E* **85** (3), 1–6.
- DOAN, Q. T., DOAN, L. T., FAROUQ ALI, S. M. & OGUZTORELI, M. 1998 Sand deposition inside a horizontal well – a simulation approach. In *Annual Technical Meeting of the Petroleum Society of Canada*, vol. 39, p. 13. Petroleum Society of Canada.
- DUBIEF, Y., TERRAPON, V. E., WHITE, C. M., SHAQFEH, E. S. G., MOIN, P. & LELE, S. K. 2005 New answers on the interaction between polymers and vortices in turbulent flows. *Flow Turbul. Combust.* **74** (4), 311–329.
- DUBIEF, Y., WHITE, C. M., TERRAPON, V. E., SHAQFEH, E. S. G., MOIN, P. & LELE, S. K. 2004 On the coherent drag-reducing and turbulence-enhancing behaviour of polymers in wall flows. *J. Fluid Mech.* **514**, 271–280.
- EINARSSON, J., YANG, M. & SHAQFEH, E. S. G. 2018 Einstein viscosity with fluid elasticity. *Phys. Rev. Fluids* **3** (1), 013301.
- FERRANTE, A. & ELGHOBASHI, S. 2003 On the physical mechanisms of two-way coupling in particle-laden isotropic turbulence. *Phys. Fluids* **15** (2), 315–329.
- FORNARI, W., FORMENTI, A., PICANO, F. & BRANDT, L. 2016 The effect of particle density in turbulent channel flow laden with finite size particles in semi-dilute conditions. *Phys. Fluids* **28** (3).
- FRANK, X. & LI, H. Z. 2006 Negative wake behind a sphere rising in viscoelastic fluids: a lattice Boltzmann investigation. *Phys. Rev. E* **74** (5), 1–9.
- GLOWINSKI, R., PAN, T. W., HESLA, T. I., JOSEPH, D. D. & PÉRIAUX, J. 2001 A fictitious domain approach to the direct numerical simulation of incompressible viscous flow past moving rigid bodies: application to particulate flow. *J. Comput. Phys.* **169** (2), 363–426.
- GOYAL, N. & DERKSEN, J. J. 2012 Direct simulations of spherical particles sedimenting in viscoelastic fluids. *J. Non-Newtonian Fluid Mech.* **183–184**, 1–13.
- GRECO, F., D'AVINO, G. & MAFFETTONE, P. L. 2007 Rheology of a dilute suspension of rigid spheres in a second order fluid. *J. Non-Newtonian Fluid Mech.* **147** (1–2), 1–10.
- HAMEDUDDIN, I., GAYME, D. F. & ZAKI, T. A. 2019 Perturbative expansions of the conformation tensor in viscoelastic flows. *J. Fluid Mech.* **858**, 377–406.
- HAMEDUDDIN, I., MENEVEAU, C., ZAKI, T. A. & GAYME, D. F. 2018 Geometric decomposition of the conformation tensor in viscoelastic turbulence. *J. Fluid Mech.* **842**, 395–427.
- HAMEDUDDIN, I. & ZAKI, T. A. 2019 The mean conformation tensor in viscoelastic turbulence. *J. Fluid Mech.* **865**, 363–380.
- HETSRONI, G. & ROZENBLIT, R. 1994 Heat transfer to a liquid–solid mixture in a flume. *Intl J. Multiphase Flow* **20** (4), 671–689.
- HUANG, P. Y., FENG, J., HU, H. H. & JOSEPH, D. D. 1997 Direct simulation of the motion of solid particles in Couette and Poiseuille flows of viscoelastic fluids. *J. Fluid Mech.* **343**, 73–94.
- KAFTORI, D., HETSRONI, G. & BANERJEE, S. 1994 Funnel-shaped vortical structures in wall turbulence. *Phys. Fluids* **6** (9), 3035–3050.
- KARNIS, A. & MASON, S. G. 1966 Particle motions in sheared suspensions. XIX. Viscoelastic media. *Trans. Soc. Rheol.* **10** (2), 571–592.

- KEMIHA, M., FRANK, X., PONCIN, S. & LI, H. Z. 2006 Origin of the negative wake behind a bubble rising in non-Newtonian fluids. *Chem. Engng Sci.* **61** (12), 4041–4047.
- KIDANEMARIAM, A. G., CHAN-BRAUN, C., DOYCHEV, T. & UHLMANN, M. 2013 Direct numerical simulation of horizontal open channel flow with finite-size, heavy particles at low solid volume fraction. *New J. Phys.* **15**, 025031.
- KIM, K., ADRIAN, R. J., BALACHANDAR, S. & SURESHKUMAR, R. 2008 Dynamics of hairpin vortices and polymer-induced turbulent drag reduction. *Phys. Rev. Lett.* **100**, 134504.
- KIM, K. & SURESHKUMAR, R. 2013 Spatiotemporal evolution of hairpin eddies, Reynolds stress, and polymer torque in polymer drag-reduced turbulent channel flows. *Phys. Rev. E* **87**, 063002.
- LASHGARI, I., PICANO, F., BREUGEM, W. P. & BRANDT, L. 2016 Channel flow of rigid sphere suspensions: particle dynamics in the inertial regime. *Intl J. Multiphase Flow* **78**, 12–24.
- LEE, J., JUNG, S. Y., SUNG, H. J. & ZAKI, T. A. 2013 Effect of wall heating on turbulent boundary layers with temperature-dependent viscosity. *J. Fluid Mech.* **726**, 196–225.
- LEE, S. J. & ZAKI, T. A. 2017 Simulations of natural transition in viscoelastic channel flow. *J. Fluid Mech.* **820**, 232–262.
- LI, G., MCKINLEY, G. H. & ARDEKANI, A. M. 2015 Dynamics of particle migration in channel flow of viscoelastic fluids. *J. Fluid Mech.* **785**, 486–505.
- LI, G. J., KARIMI, A. & ARDEKANI, A. M. 2014 Effect of solid boundaries on swimming dynamics of microorganisms in a viscoelastic fluid. *Rheol. Acta* **53** (12), 911–926.
- LIM, E. J., OBER, T. J., EDD, J. F., DESAI, S. P., NEAL, D., BONG, K. W., DOYLE, P. S., MCKINLEY, G. H. & TONER, M. 2014 Inertio-elastic focusing of bioparticles in microchannels at high throughput. *Nat. Commun.* **5**, 4120.
- LOISEL, V., ABBAS, M., MASBERNAT, O. & CLIMENT, E. 2013 The effect of neutrally buoyant finite-size particles on channel flows in the laminar-turbulent transition regime. *Phys. Fluids* **25** (12), 123304.
- LUCCI, F., FERRANTE, A. & ELGHOBASHI, S. 2011 Is Stokes number an appropriate indicator for turbulence modulation by particles of Taylor-length-scale size? *Phys. Fluids* **23** (2), 025101.
- LUMLEY, J. L. 1969 Drag reduction by additives. *Annu. Rev. Fluid Mech.* **1** (1), 367–384.
- MARCHIOLI, C. & SOLDATI, A. 2002 Mechanisms for particle transfer and segregation in a turbulent boundary layer. *J. Fluid Mech.* **468**, 283–315.
- MATAS, J. P., MORRIS, J. F. & GUZZELLI, E. 2004 Inertial migration of rigid spherical particles in Poiseuille flow. *J. Fluid Mech.* **515**, 171–195.
- MORRIS, J. F. 2009 A review of microstructure in concentrated suspensions and its implications for rheology and bulk flow. *Rheol. Acta* **48** (8), 909–923.
- NASO, A. & PROSPERETTI, A. 2010 The interaction between a solid particle and a turbulent flow. *New J. Phys.* **12**, 033040.
- NICOLAOU, L., JUNG, S. Y. & ZAKI, T. A. 2015 A robust direct-forcing immersed boundary method with enhanced stability for moving body problems in curvilinear coordinates. *Comput. Fluids* **119**, 101–114.
- NOWBAHAR, A., SARDINA, G., PICANO, F. & BRANDT, L. 2013 Turbophoresis attenuation in a turbulent channel flow with polymer additives. *J. Fluid Mech.* **732**, 706–719.
- PAGE, J. & ZAKI, T. A. 2014 Streak evolution in viscoelastic Couette flow. *J. Fluid Mech.* **742**, 520–521.
- PAGE, J. & ZAKI, T. A. 2015 The dynamics of spanwise vorticity perturbations in homogeneous viscoelastic shear flow. *J. Fluid Mech.* **777**, 327–363.
- PAN, Y. & BANERJEE, S. 1996 Numerical simulation of particle interactions with wall turbulence. *Phys. Fluids* **8** (10), 2733–2755.
- PAN, Y. & BANERJEE, S. 1997 Numerical investigation of the effects of large particles on wall-turbulence. *Phys. Fluids* **9** (12), 3786–3807.
- PICANO, F., BREUGEM, W. P. & BRANDT, L. 2015 Turbulent channel flow of dense suspensions of neutrally buoyant spheres. *J. Fluid Mech.* **764**, 463–487.
- POPE, S. B. 2000 *Turbulent Flows*, vol. 12. Cambridge University Press.
- READE, W. C. & COLLINS, L. R. 2000 Effect of preferential concentration on turbulent collision rates. *Phys. Fluids* **12** (10), 2530–2540.

- ROSENFELD, M., KWAK, D. & VINOKUR, M. 1991 A fractional step solution method for the unsteady incompressible Navier–Stokes equations in generalized coordinate systems. *J. Comput. Phys.* **94** (1), 102–137.
- SCIROCCO, R., VERMANT, J. & MEWIS, J. 2005 Shear thickening in filled Boger fluids. *J. Rheol.* **49** (2), 551–567.
- SEGRE, G. & SILBERBERG, A. 1961 Radial particle displacements in Poiseuille flow of suspensions. *Nature* **189** (4760), 209–210.
- SHAO, X., WU, T. & YU, Z. 2012 Fully resolved numerical simulation of particle-laden turbulent flow in a horizontal channel at a low Reynolds number. *J. Fluid Mech.* **693**, 319–344.
- SHAW, R. 2003 Particle-turbulence interactions in atmospheric clouds. *Annu. Rev. Fluid Mech.* **35**, 183–227.
- SILBERMAN, E. 1983 The effect of drag-reducing additives on fluid flows and their industrial applications part 1: basic aspects. *J. Hydraul Res.* **21** (1), 72–73.
- SNIJKERS, F., D’AVINO, G., MAFFETTONE, P. L., GRECO, F., HULSEN, M. A. & VERMANT, J. 2011 Effect of viscoelasticity on the rotation of a sphere in shear flow. *J. Non-Newtonian Fluid Mech.* **166** (7–8), 363–372.
- TAMANO, S., GRAHAM, M. D. & MORINISHI, Y. 2011 Streamwise variation of turbulent dynamics in boundary layer flow of drag-reducing fluid. *J. Fluid Mech.* **686** (10), 352–377.
- TOMS, B. A. 1948 Some observations on the flow of linear polymer solutions through straight tubes at large Reynolds numbers. In *Proceedings of the 1st International Congress on Rheology*, pp. 135–141. North-Holland.
- UHLMANN, M. 2005 An immersed boundary method with direct forcing for the simulation of particulate flows. *J. Comput. Phys.* **209** (2), 448–476.
- UHLMANN, M. & DOYCHEV, T. 2014 Sedimentation of a dilute suspension of rigid spheres at intermediate Galileo numbers: the effect of clustering upon the particle motion. *J. Fluid Mech.* **752** (2), 310–348.
- VAITHIANATHAN, T., ROBERT, A., BRASSEUR, J. G. & COLLINS, L. R. 2006 An improved algorithm for simulating three-dimensional, viscoelastic turbulence. *J. Non-Newtonian Fluid Mech.* **140** (1–3), 3–22.
- VIRK, P. S., MICKLEY, H. S. & SMITH, K. A. 1970 The ultimate asymptote and mean flow structure in Toms’ phenomenon. *Trans. ASME J. Appl. Mech.* **2** (37), 488–493.
- WANG, G., ABBAS, M. & CLIMENT, E. 2018 Modulation of the regeneration cycle by neutrally buoyant finite-size particles. *J. Fluid Mech.* **852**, 257–282.
- WANG, S. N., SHEKAR, A. & GRAHAM, M. D. 2017 Spatiotemporal dynamics of viscoelastic turbulence in transitional channel flow. *J. Non-Newtonian Fluid Mech.* **244**, 104–122.
- WHITE, C. M., DUBIEF, Y. & KLEWICKI, J. 2018 Properties of the mean momentum balance in polymer drag-reduced channel flow. *J. Fluid Mech.* **834**, 409–433.
- WHITE, C. M. & MUNGAL, M. G. 2008 Mechanics and prediction of turbulent drag reduction with polymer additives. *Annu. Rev. Fluid Mech.* **40** (1), 235–256.
- XI, L. & GRAHAM, M. D. 2010 Active and hibernating turbulence in minimal channel flow of newtonian and polymeric fluids. *Phys. Rev. Lett.* **104**, 218–301.
- XI, L. & GRAHAM, M. D. 2012 Intermittent dynamics of turbulence hibernation in Newtonian and viscoelastic minimal channel flows. *J. Fluid Mech.* **693**, 433–472.
- YEO, K. & MAXEY, M. R. 2011 Numerical simulations of concentrated suspensions of monodisperse particles in a Poiseuille flow. *J. Fluid Mech.* **682**, 491–518.
- YU, Z., LIN, Z., SHAO, X. & WANG, L. P. 2017 Effects of particle-fluid density ratio on the interactions between the turbulent channel flow and finite-size particles. *Phys. Rev. E* **96** (3), 1–15.
- ZADE, S., LUNDELL, F. & BRANDT, L. 2019 Turbulence modulation by finite-size spherical particles in Newtonian and viscoelastic fluids. *Intl J. Multiphase Flow* **112**, 116–129.
- ZENIT, R. & FENG, J. J. 2018 Hydrodynamic interactions among bubbles, drops, and particles in non-Newtonian liquids. *Annu. Rev. Fluid Mech.* **50** (1), 505–534.
- ZHANG, Q. & PROSPERETTI, A. 2010 Physics-based analysis of the hydrodynamic stress in a fluid-particle system. *Phys. Fluids* **22** (3), 6–17.